EFFECT OF LOADING RATE ON TENSILE STRENGTH OF MAHA SARAKHAM SALT WITH VARIOUS CARNALLITE CONTENTS

Monyapat Chobsranoi

มหาวิทยาลัยเทคโนโลยีสุรนารี

A Thesis Submitted in Partial Fulfillment of the Requirements for the

Degree of Master of Engineering in Geotechnology

Suranaree University of Technology

Academic Year 2016

ผลกระทบของอัตราการให้แรงต่อกำลังรับแรงดึงของเกลือหินชุดมหาสารคาม ภายใต้การผันแปรของปริมาณแร่คาร์นัลไลต์

นางสาวมนญ์ญพัชญ์ ชอบสระน้อย

มหาวิทยาลัยเทคโนโลยีสุรนารี

วิทยานิพนธ์นี้เป็นส่วนหนึ่งของการศึกษาตามหลักสูตรปริญญาวิศวกรรมศาสตรมหาบัณฑิต
สาขาวิชาเทคโนโลยีธรณี
มหาวิทยาลัยเทคโนโลยีสุรนารี
ปีการศึกษา 2559

EFFECT OF LOADING RATE ON TENSILE STRENGTH OF MAHA SARAKHAM SALT WITH VARIOUS CARNALLITE CONTENTS

Suranaree University of Technology has approved this thesis submitted in partial fulfillment of the requirements for a Master's Degree.

Thesis Examining Committee

_____

(Asst. Prof. Dr. Helmut Durrast)

Chairperson

_____

(Asst. Prof. Dr. Decho Phueakphum)

Member (Thesis Advisor)

_____

(Prof. Dr. Kittitep Fuenkajorn)

Member

_____ _____

(Prof. Dr. Sukit Limpijumnong) (Assoc. Prof. Flt. Lt. Dr. Kontorn Chamniprasart)

Vice Rector for Academic Affairs and Innovation

Dean of Institute of Engineering

มหาวิทยาลัยเทคโนโลยีสุรนารี

มนญ์ญพัชญ์ ชอบสระน้อย : ผลกระทบของอัตราการให้แรงต่อกำลังรับแรงดึงของเกลือหินชุดมหาสารคามภายใต้การผันแปรของปริมาณแร่คาร์นัลไลต์
(EFFECT OF LOADING RATE ON TENSILE STRENGTH OF MAHA SARAKHAM SALT WITH VARIOUS CARNALLITE CONTENTS) อาจารย์ที่ปรึกษา : ผู้ช่วยศาสตราจารย์ ดร.เดโช เผือกภูมิ, 89 หน้า

การทดสอบการดัดงอแบบสี่จุดได้ดำเนินการทดสอบในห้องปฏิบัติการบนตัวอย่างเกลือหินที่มีแร่คาร์นัลไลต์ผันแปรตั้งแต่ร้อยละ 0 ถึง 95 โดยน้ำหนัก อัตราการให้แรงดึงมีค่าคงที่เท่ากับ 10^{-6} ถึง 10^{-3} เมกะปาสคาลต่อวินาที ผลการทดสอบระบุว่าค่ากำลังรับแรงดึงมีค่าลดลงเมื่อปริมาณแร่คาร์นัลไลต์เพิ่มขึ้นและอัตราการให้แรงดึงลดลง สมการความสัมพันธ์ระหว่างพลังงานความเครียดที่จุดแตก (W) ในฟังก์ชันของปริมาณแร่คาร์นัลไลต์ ($C_{\%}$) สามารถคำนวณได้จากสมการ $W = 2.17 \exp[-0.03 C_{\%}]$ กิโลปาสคาลต่อวินาที ค่าตัวแปรเชิงคณิตศาสตร์ในสมการของแมกซ์เวลได้จากการสอบเทียบของแผนภูมิความสัมพันธ์ระหว่างความเครียดดึงในเชิงเวลาจากการทดสอบในห้องปฏิบัติการ โปรแกรม FLAC ได้นำมาใช้จำลองช่องเหมืองในชั้นเกลือหินภายใต้การผันแปรความลึกและความกว้างของช่องเหมือง การคำนวณความเค้นที่หลังคาร่วมกับเกณฑ์พลังงานความเครียดได้ถูกนำมาใช้เพื่อหาความเครียดดึงที่จุดวิกฤต โดยระยะเวลาสูงสุดที่ช่องเหมืองยังคงมีเสถียรภาพโดยไม่ต้องมีการค้ำยันสามารถคาดการณ์ได้จากการแทนที่ค่าความเครียดที่จุดวิกฤติลงในแผนภูมิความสัมพันธ์ระหว่างความเครียดและเวลา

มหาวิทยาลัยเทคโนโลยีสุรนารี

สาขาวิชา เทคโนโลยีธรณี ลายมือชื่อนักศึกษา_____

ปีการศึกษา 2559 ลายมือชื่ออาจารย์ที่ปรึกษา_____

MONYAPAT CHOBSRANOI : EFFECT OF LOADING RATE ON TENSILE STRENGTH OF MAHA SARAKHAM SALT WITH VARIOUS CARNALLITE CONTENTS. THESIS ADVISOR : ASST. PROF. DECHO PHUEAKPHUM, Ph.D., 89 PP.

TENSILE STRENGTH/CARNALLITE/BENDING TEST/CREEP/SPAN

Four-point bending tests are performed on prismatic beams of potash specimens with carnallite contents ranging from 0 to 95%. The applied loading rates are maintained constant, which are equivalent to the induced tensile stress rates at the crack initiation point ranging from 10^{-6} to 10^{-3} MPa/s. The tensile strengths (σ_t) decrease when the carnallite contents ($C_{\%}$) increase and the stress rates decrease. The strain energy at failure (W) has been calculated and derived as a function of $C_{\%}$, which can be described by: $W = 2.17 \cdot \exp[-0.03\, C_{\%}]$ kPa. The Maxwell model parameters are calibrated by regression analysis of the test results, and hence series of tensile strain-time curves can be constructed for various applied tensile stresses. The maximum tensile stresses induced in the mine roof are calculated using FLAC program for various depths and room widths. The calculated roof stresses combining with the strain energy criterion are used to determine the critical tensile strain that the roof can sustain before failure occurs. By substituting the critical strain into the strain-time curves the standup time can be predicted.

School of Geotechnology Student's Signature _____

Academic Year 2016 Advisor's Signature _____

ACKNOWLEDGMENTS

I wish to acknowledge the funding supported by Suranaree University of Technology (SUT).

I would like to express my sincere thanks to Prof. Dr. Kittitep Fuenkajorn for his valuable guidance and efficient supervision. I appreciate his strong support, encouragement, suggestions and comments during the research period. My heartiness thanks to Assoc. Prof. Dr.Helmut Durrast, Asst. Prof. Dr. Decho Phueakphum and Dr. Prachya Tepnarong for their constructive advice, valuable suggestions and comments on my research works as thesis committee members. Grateful thanks are given to all staffs of Geomechanics Research Unit, Institute of Engineering who supported my work.

Finally, I would like to thank beloved parents for their love, support and encouragement.

Monyapat Chobsranoi

มหาวิทยาลัยเทคโนโลยีสุรนารี

TABLE OF CONTENTS

Page

TABLE OF CONTENTS (Continued)

Page

TABLE OF CONTENTS (Continued)

Page

TABLE OF CONTENTS (Continued)

Page

มหาวิทยาลัยเทคโนโลยีสุรนารี

LIST OF TABLES

Table **Page**

มหาวิทยาลัยเทคโนโลยีสุรนารี

LIST OF FIGURES

Figure **Page**

LIST OF FIGURES (Continued)

Figure **Page**

LIST OF FIGURES (Continued)

Figure **Page**

LIST OF FIGURES (Continued)

Figure **Page**

มหาวิทยาลัยเทคโนโลยีสุรนารี

SYMBOLS AND ABBREVIATIONS

σ_t	=	Tensile stresses
σ_T	=	Stress
σ_R	=	Constant stress rate
$\sigma_1, \sigma_2, \sigma_3$	=	Principal stresses
ε	=	Strain
ε_t	=	Tensile strain
$\varepsilon_1, \varepsilon_2, \varepsilon_3$	=	Principal strain
P	=	Load
L	=	Support span
b	=	Specimen width
d	=	Specimen thickness
t	=	Time
E, E_1	=	Elastic modulus
E_2	=	Spring constant in visco-elastic phase
η	=	Viscosity parameter
η_1	=	Visco-plastic coefficient in steady-state phase
η_2	=	Visco-elastic coefficient in transient phase
ρ	=	Density
ϕ	=	Friction angle
W	=	Strain energy density

มหาวิทยาลัยเทคโนโลยีสุรนารี

SYMBOLS AND ABBREVIATIONS (Continued)

W_t	=	Strain energy from four-point bedding test
W_o	=	Room width
K	=	Bulk modulus
G	=	Shear modulus
c	=	Cohesion
$C_{\%}$	=	Carnallite contents
$\partial\sigma/\partial t$	=	Constant stress rate
$\delta\cdot$	=	Empirical constant for equation (5.2)
δ'	=	Empirical constant for equation (5.2)
ω	=	Empirical constant for equation (5.3)
ω'	=	Empirical constant for equation (5.3)
α	=	Empirical constant for equation (5.4)
α'	=	Empirical constant for equation (5.4)
χ	=	Empirical constant for equation (5.4)
λ	=	Empirical constant for equation (5.8)
κ	=	Empirical constant for equation (5.8)
φ	=	Empirical constant for equation (7.2)
φ'	=	Empirical constant for equation (7.2)
ζ	=	Empirical constant for equation (7.2)

มหาวิทยาลัยเทคโนโลยีสุรนารี

CHAPTER I

INTRODUCTION

1.1 Background and rationale

Tensile strength of rock dictate the maximum span and standup time of the mine opening in stratified rock mass. The tensile strength can be obtained in the laboratory by various methods, including direct tension tests, Brazilian tension tests, ring tension tests, flexural tests, three- and four-point bending tests (Phueakphum et al., 2013; Wisetsaen et al., 2014). For the analysis and design of the mine roof span the bending test is more preferable than the others because the bending test specimen is subject to the stress configurations similar to those in the mine roof. The design of the mine roof span for brittle rock is normally consider the fracture characteristics (shear strength, spacing, water pressure, etc.). For soft and time-dependent rocks, such as rock salt and potash, the design considerations should also be placed on the time-dependent strength and deformation of the materials.

1.2 Research objectives

The objective of this study is to determine the time-dependent tensile strengths of rock salt with various carnallite contents. The four-point bending tests are performed on prismatic beams (50×50×200 mm) of rock salt specimens with carnallite contents ranging from 0 to 95%. The applied loading rates are various which are equivalent to the tensile stress rates of 10^{-6} to 10^{-3} MPa/s. They are loaded axially at a constant rate

of 0.045 N/s to 45 N/s until failure occurs. The specimen deformations are monitored with strain gages to calculate the tensile strains. The tensile strains are monitored at the point where the incipient tensile crack is induced. The results is used to determine the maximum unsupported span and standup time of potash mine roof. The Maxwell model is used to describe the time-dependent tensile strain of the specimens. Its elastic and visco-plastic parameters are calibrated by regression analysis of the test results, and hence series of tensile strain-time curves can be constructed for various applied tensile stresses. The maximum tensile stresses induced in the mine roof are calculated using FLAC program for various depths and room widths (spans). The local regulations require that the roof thickness is not less than 40% of the room width because the potash layer lies under relatively soft claystone. The calculated roof stresses combining with the strain energy criterion are used to determine the critical tensile strain that the roof can sustain before failure occurs. By substituting the critical strain into the strain-time curves the standup time can be predicted.

1.3 Scope and Limitations

The scope and limitations of the research include as follows.

1) All specimens are conducted on rock specimens obtained from the Maha Sarakham formation (ASEAN Potash Mining Co., Ltd. (APMC)).
2) The nominal dimensions of prismatic blocks are 50×50×200 mm.
3) The applied loading rates vary from 10^{-6} to 10^{-3} MPa/s.
4) The testing procedures follow the relevant ASTM standard practices.
5) Finite difference analyses (FLAC 4.0) used to determine the maximum tensile stresses in the mine roof.

6) The research findings are published in conference paper or journal.

1.4 Research methodology

The research methodology shown in Figure 1.1 comprises 9 steps; including literature review, sample preparation, four-point bending testing, strength criterion and salt properties calibration, analysis and assessment, numerical method, application, discussions and conclusions and thesis writing.

1.4.1 Literature review

Literature review is carried out to study researches about tensile strength, loading rate and four-point bending tests. The sources of information are from journals, technical reports and conference papers. A summary of the literature review is given in the thesis.

1.4.2 Sample preparation

Rock samples used here have been obtained from underground openings of ASEAN Potash Mining Co., Ltd. (APMC). They belong to the Lower Salt member of the Maha Sarakham formation. Sample preparation is carried out in the laboratory at Suranaree University of Technology. The specimens have been prepared to obtain prismatic blocks with nominal dimensions of 50×50×200 mm.

1.4.3 Laboratory testing

The laboratory testing includes four-point bending tests following ASTM D6272-10. A data logger (TC-32K) connected with the switching box (Type B-2760) is used to monitor the induced tensile strains. The loads apply under four constant rates from 0.045 N/s to 45 N/s, which are equivalent to the induced tensile stressed rates at the center of the specimen from 10^{-6} to 10^{-3} MPa/s. The load at failure

is recorded to calculate the tensile strength. Photographs are taken of the failed specimens.

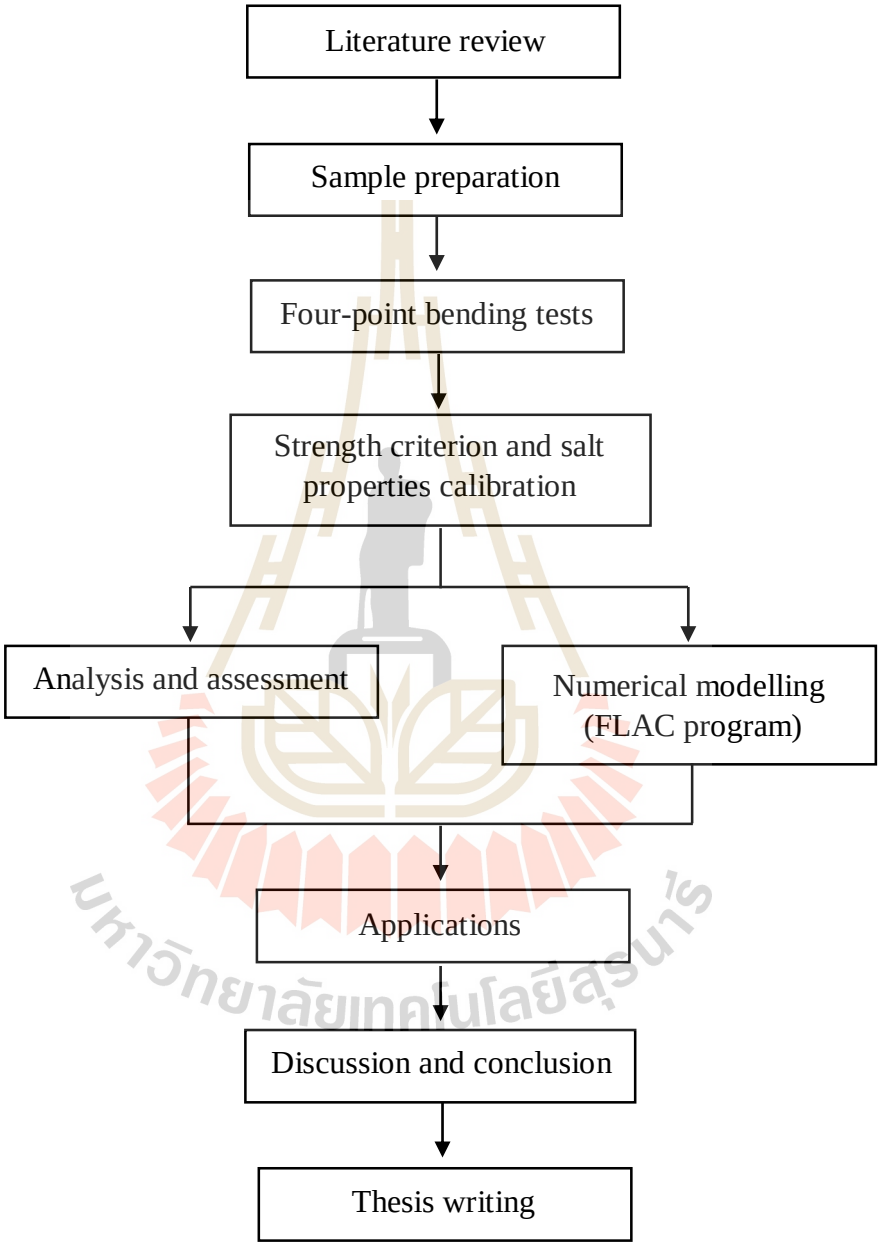

Figure 1.1 Research Methodology.

1.4.4 Strength criterion and salt properties calibration

The results is used to calibrate the elastic and visco-elastic parameters of the salt rock. It is assumed here that the salt behavior can be described by the Maxwell model. The regression analysis on the linear visco-elastic equation is made on the test data. Results from laboratory measurements in terms of the tensile strength of rock salt under various carnallite contents and loading rates are also be used to formulate mathematical relations.

1.4.5 Analysis and assessment

The results of the test are presented in forms of the tensile strength and the tensile strains at failure. The Maxwell model is used to describe the time-dependent tensile strain of the salt specimens under various carnallite content.

1.4.6 Numerical modelling (FLAC program)

A finite difference analysis with the creep model above is performed to simulation mine roof in rock salt to determine the maximum tensile stresses and tensile strains for each roof widths, depths and $C_{\%}$ from 0%, 20%, 40%, 60%, 80% to 100%. The analysis is made in plane strain condition.

1.4.7 Applications

The laboratory testing and numerical analysis can be applied to the mine roof in potash to determine the maximum unsupported span and standup time. Numerical simulations of the mine roof under different of roof width, depth, and $C_{\%}$ can provide the maximum tensile stress in the middle of the salt roof. The calculate roof stress combining with the strain energy criterion is used to determine the critical tensile strain that the roof can sustain before failure occurs. By substituting the critical strain into the strain-time curves the standup time can be predicted.

1.4.8 Discussions and conclusions

Discussions are made on the reliability and adequacies of the approaches used here. Future research needs are identified. All research activities, methods, and results are documented and complied in the thesis. The research or findings are published in the conference proceedings or journals.

1.4.9 Thesis writing

All study activities, methods, and results are documented and complied in the thesis.

1.5 Thesis content

This research thesis is divided into eight chapters. The first chapter includes background and rationale, research objectives, scope and limitations and research methodology. The second chapter presents results of the literature review about tensile strength, loading rate, Four-point bending tests and numerical modeling. The chapter three describes sample preparation. The laboratory testing and testing results described in chapter four. The strength criterion and salt properties calibration is explicated in chapter five. Chapter six presents the method and result of finite difference analysis using FLAC (Itasca, 1992) to simulations of the mine roof in rock salt. Chapter seven present application about underground mining and chapter eight present discussions, conclusions and recommendation for future studies.

CHAPTER II

LITERATURE REVIEW

2.1 Introduction

The topic reviewed here include basic properties of potash, basic properties of salt, tensile strength, loading rate effects, four-point bending test, and numerical method.

2.2 Basic properties of potash

Suwanich (2007) studies the potash-evaporite deposits in the northeastern portion of Thailand. The northeastern Thailand forms as the landscape of low elevation plateau (about 150-220 m. above mean sea level). This is called Khorat plateau. The Khorat plateau is divided into 2 basins, the north basin or Sakhon Nakhon basin and the south basin or Khorat basin. The potash minerals are deposited in the Maha Sarakham Formation which is the rock salt main deposits. The Maha Sarakham Formation is consisted of 3-layer salt beds, the Upper, Middle and Lower salt layers. These salt beds are interbedded by clastic sediments of sticky reddish brown mainly clay. The potash minerals have been found only at the top of the Lower Salt. There are only 2 kinds, carnallite ($KMgCl_3 \cdot 6H_2O$) and sylvite (KCl). They are usually deposited and interlocking with halite or rock salt grains and called the carnallitite and sylvite strata. The other evaporate minerals mostly found in the potash minerals are tachyhydrite

(Mg-rich mineral) and rare boracites and gypsum. The structure of the Maha Sarakham Formation varies from common salt strata to salt domes. The Lower Salt in domed up through the Middle and Upper Salt closing to the surface. The peak or highest point of the domes is leached by groundwater remaining only the salt whereas the flank around the domes still remains the potash mineral containing sylvinite mainly. The carnallite is usually found beyond the flank of the domes. The theory said that the carnallite is the primary mineral while the sylvite is the secondary deposit altered from carnallite reacting with the groundwater in suitable condition.

Weck et al. (2014) reported the functional density calculations of the structures and properties of carnallite ($KMgCl_3{\cdot}6H_2O$) possesses the orthorhombic space group *Pnna*, with Z = 12, and computed lattice parameters: a = 16:28 Å, b = 22:83 Å, c = 9:59 Å; $\alpha = \beta = \gamma = 90°$ (V = 3564.13 $Å^3$; b/a = 1:40; c/a = 0:59) shown in Figure 2.1.

Figure 2.1 Crystal unit cells of carnallite ($KMgCl_3{\cdot}6H_2O$; *Pnna*; Z = 12) optimized at the GGA/PBE level of theory. Color legend: K, purple; Ca, blue; Mg, orange; O, red; Cl, green; H, white; S, yellow (Weck et al., 2014).

The crystal structure of carnallite consists of a network of face-sharing KCl_6 octahedra and of isolated $Mg(H_2O)_6$ octahedra occupying the openings in the KCl network, with the water molecules acting as charge transmitters between $Mg^{2+}$and Cl^- ions. The computed interatomic distances are 2.06-2.09 Å for Mg-OH_2 and 3.18-3.36 Å for K-Cl forming octahedra and the H···Cl hydrogen bonds are predicted to be in the range 2.14-2.19 Å. The computed structure is about 3.0% larger than the structure characterized by Schlemper and co-workers (Schlemper et al., 1985) using XRD (Table 2.1), with good agreement found between calculated and measured axial ratios (i.e. b/a = 1:394; c/a = 0:592). The measured interatomic distances in the octahedra are 2.027-2.053 Å for Mg-OH_2 and 3.154-3.321 Å for K-Cl and the experimental H···Cl hydrogen bonds are in the range 2.255-2.429 Å.

Mellegard et al. (2012) investigated the mechanical properties of potash in the laboratory. The test specimens contained varying amounts of sylvite and carnallite. The use of X-Ray Diffraction (XRD) is costly and required destruction of the post-test sample. An alternative approach was to use the mineralogical assay result obtained by the mining company through use the X-Ray Fluorescence (XRF). Analysis of the laboratory testing data includes sorting the test result into two separate databases, one for halite and one for sylvite. Initially, the shorting of the data was bases on the bulk density of each specimen that was calculated during the specimen fabrication process. The density of halite is reported as 2.16 g/cc, while the density of sylvite is reported as 1.99 g/cc (Hurlbut and Klein (1977)). Therefore, low-density specimens assumed to be high in either sylvite or carnallite, were categorized as having a density that ranged from 1.99 to 2.11 g/cc. High-density assumed to be high in halite content, were categorized as having a density that ranged from 2.12 to 2.19 g/cc.

Table 2.1 Crystallographic data calculated at the GGA/PBE level of theory. (Hawthorne et al., 1975).

Name Sp. gp. **Z**	**Carnallite *Pnna*** **12**
a (Å)	16.28
b (Å)	22.83
c (Å)	9.59
α (◦)	90
β (◦)	90
γ (◦)	90
V (Å^3)	3564.13

2.3 Basic properties of salt

Table 2.2 summarizes the basic properties of rock salt from the laboratory tests from various sources.

Table 2.2 Density of halite minerals at ordinary temperature and pressure.

Mineral	**Density, gm/cm^3**	**References**
NaCl (halite)	2.14	Birch et al. (1942)
	2.17	Heiland (1940), Hodgman et al. (1955-1956)
	2.16	Straumanis (1953)
	2.16	Sathe et al. (1945)
	2.16	Batuecas and Carreirra (1955)
	2.16	Forsythe (1954)
	2.16	Johnston and Hutchison (1942)
	2.15	Bacher (1949)
	2.16	National Research council of the U.S.A. (1929)
Average : NaCl (halite)	2.16	

มหาวิทยาลัยเทคโนโลยีสุรนารี

2.4 Tensile strength

Weinberger (1994) discusses the tensile strength and elastic properties of rock which are measured with a four-point beam device placed inside a pressure vessel. The result indicates that almost all strain-stress curves display irregular curves of σ_t and σ_c for tensile strain larger than 0.0001 to 0.0003, the irregularities increase with increasing strain. They interpret these irregularities as local, stable fracturing. These fractures initiate at the tensile surface of the beam, where the tensile stress are the highest and they propagate into the inner part of the beam. These early fractures grow stably, and they are arrested as they approach the neutral surface of the beam. Eventually, the sample fails at the ultimate stress. The tensile Young's modulus is nonlinear and best represented by $\sigma_t = A\varepsilon_t^B$, where σ_t, ε_t are tensile stress and tensile strain and A and B are constants. B ranges from 0.56 for test without confinement to 0.85-0.9 for test with confinement of 10 MPa or more.

Jager et al. (2007) state that values of the tensile strength determined form bending test on rock are significantly greater than the uniaxial tensile strength. While this effect are not understood, it is well recognized, and the term modulus of rupture is used for the extreme tensile stress determined form a bending test. Obert et al. (1946) include three-point bending of 6-in. length of drill core in their standardized test for studying mine rock, and Pomeroy and Morgans (1956), Berenbaum and Brodie (1959), and Evans (1961) have used bending to study the tensile strength of coal, which is, of course, extremely difficult to test in direct uniaxial tension. Fairhurst (1961) discusses the effects of difficult value for Young's modulus in tension and compression on bending test and describes apparatus for four-point

loading. Bending is the simplest method of studying time-dependent behavior of rock, such as creep, and has been used for this purpose by Price and Cosgrove (1964).

Liu et al. (2010) used MTS815 Flex text GT rock mechanics test system and PCI-II three-dimensional acoustic emission test system to study the damage and fractal characteristics of tensile failure in bedded salt rock are studied under indirect and direct tensile test conditions. The tensile strength as well as the correlation between indirect strength and direct tensile strength are obtained. Under indirect and direct tensile test conditions, the spatial distribution of acoustic emission and the damage evolution trend are derived for each stress stage during the full failure process. Based on the fractal column covering method, the fractal characteristic of acoustic emission spatial distribution in rock damage under indirect and direct tensile test conditions are studied. The test results indicate that indirect tensile strength of interlayer salt rock are higher than of pure salt rock and direct tensile strength of pure salt rock are much lower than that of the indirect tensile strength. From the tensile strength difference between the indirect and direct tensile test and failure states, can tell that the tensile strength value from direct tensile test compared with the one from indirect strength test is closer to the virtual strength properties of salt rock. The research results show that with fracture dimensions of damage spatial distribution increasing, the tensile stress decreases following negative exponential law.

Forster (1967) discusses three different tests were conducted in order to determine the tensile strength of the rock salt these were the direct, indirect and beam tests. The results of the beam tests (three point, four point and uniformly loaded) are in general higher than those from the Brazilian disc tests. Figure 2.2 also confirms that the tensile strength is an exponential function of the length/height ratio of the salt beam.

However, the beam test results (all tests) showed a significant variation depending on the beam geometry and the petrology, between 0.62 MPa and 6.21 MPa, which is far more pronounced than the Brazilian test results. Clearly, this is a function of the nature of the tests, as the presence of slight flaws within the specimen will affect the failure load, thereby highlighting the need for accurate specimen preparation. Also, as the length of the specimen is increased there is a greater chance of including mechanical defects within the sample.

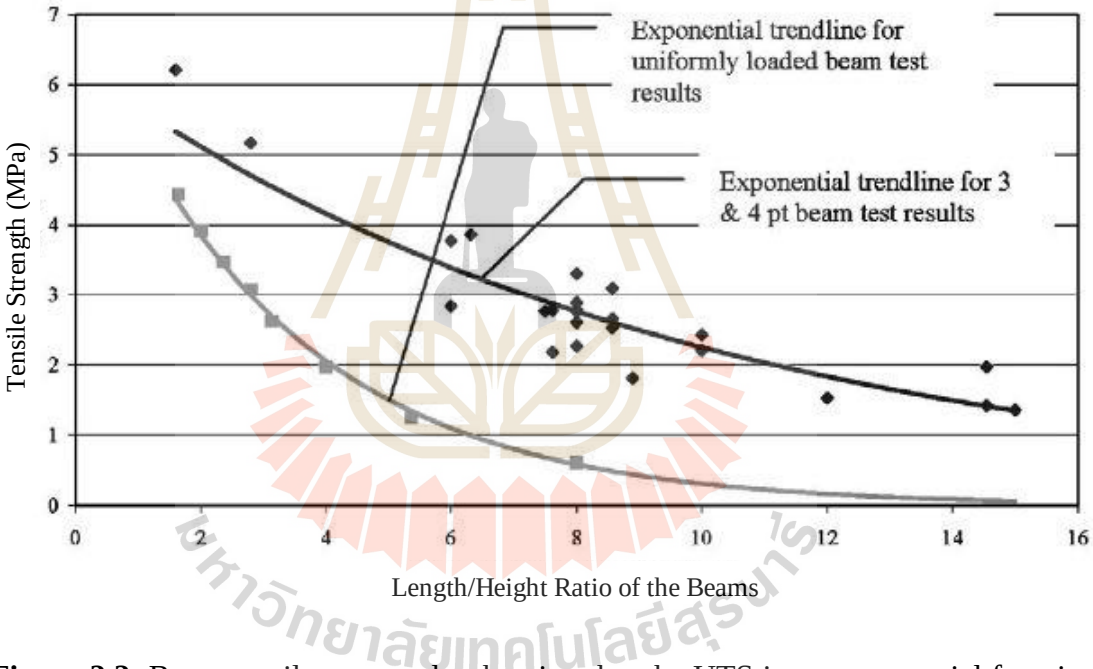

Figure 2.2 Beam tensile test results showing that the UTS is an exponential function of the beam length/height ratio (Forster, 1967).

2.5 Loading rate effects

Zhang and Wong (2014) discuss the loading mechanisms associated with different loading rates in the Bonded-particle model (BPM) and examines the numerical outputs under these different rates for used in which calibration against the results from Brazilian tensile tests have been commonly conducted. The specimens in the numerical analysis of the Brazilian tensile tests are subjected to vertical loading applied at six different loading rates: 0.005, 0.01, 0.02, 0.08, 0.2 and 0.6 m/s. The induced tensile stress σ_t is calculated as follows:

$$\sigma_t = F / \pi Rt \tag{2.1}$$

where F is the compressive force acting on the platens, R and t are the radius and thickness of the Brazilian disk, respectively.

The peak value of the induced tensile stress is the Brazilian tensile strength of the test specimen. The results from the Brazilian tensile tests indicate that the Brazilian tensile strength (σ_t) increase as the loading rate increases.

Wisetsaen et al. (2015) studied the effects of loading rate and temperature on tensile strength and deformation of rock salt. To determine the time-dependent tensile strength and deformability of the Maha Sarakham salt under temperatures ranging from 273 to 375 K. The ring tension tests are performed under various loading rates which are equivalent to the tensile stress rates induced at the crack initiation point of 3×10^{-5}, 3×10^{-4}, 3×10^{-3}, 3×10^{-2} and 3×10^{-1} MPa/s. The results indicate that the tensile strength increases with the loading rate, and decreases with increasing temperatures.

2.6 Bending test

2.6.1 Three-point bending test

The American Society for Testing and Materials (ASTM (C293–02)) specifies the methods and sample preparation for the three-point bending test. All forces are be applied perpendicular to the face of the specimen continuously without eccentricity. A diagram of an apparatus that accomplishes this purpose is shown in Figure 2.3. The load is applied at a constant rate to the breaking point. The maximum stress on the tension face increases under loading rate between 0.9 and 1.2 MPa/min (125 and 175 psi/min). The loading rate is calculated using the following equation:

$$r = 2Sbd^2 / 3L \tag{2.2}$$

where r is loading rate, N/min (lb/min), S is rate of increase in the maximum stress on the tension face, MPa/min (psi/min), b is average width of the specimen as oriented for testing, mm (in), d is average depth of the specimen as oriented for testing, mm (in.) and L is span length, mm (in).

The modulus of rupture is calculated as follows:

$$R = 3PL / 2bd^2 \tag{2.3}$$

where R is modulus of rupture, MPa (psi), P is maximum applied load indicated by the testing machine, N (lbf), L is span length, mm (in.), b is average width of specimen, at the fracture, mm (in.) and d is average depth of specimen, at the fracture, mm (in.). A bar of rectangular cross section rests on two supports and is loaded at two points or

two loading noses. The distance between the loading noses (the load span) is either one third or one half of the support span.

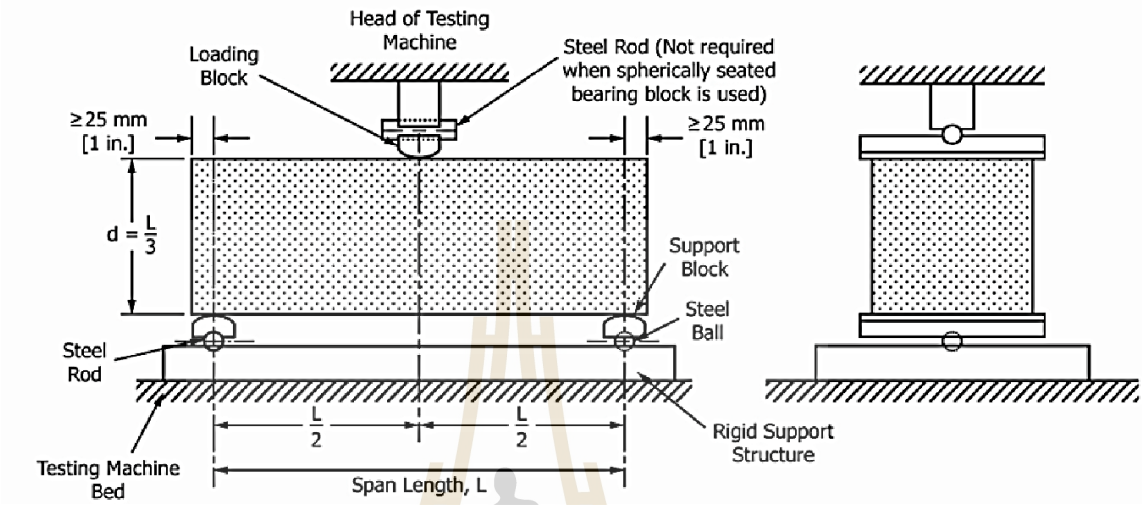

Figure 2.3 Schematic of a suitable apparatus for flexure test by center-point loading method (ASTM C293–02).

2.6.2 Four-point bending test

Specifications for standard test method for four-point bending test by American Society for Testing and Materials ASTM (D6272 – 02). The test method is a bar of rectangular cross section rests on two supports and is loaded at two points or two loading noses, each an equal distance from the adjacent support point. The distance between the loading noses (the load span) is either one third or one half of the support span shown in Figure 2.4.

When a beam is loaded in flexure at two central points and supported at two outer points, the maximum stress in the outer fibers occurs between the two central loading points that define the load span. This stress may be calculated for any point on

the load deflection curve for relatively small deflections by the following equation for a load span of one third of the support span:

$$S = PL / bd^2 \quad (2.4)$$

For a load span of one half of the support span:

$$S = 3PL / 4bd^2 \quad (2.5)$$

where S is stress in the outer fiber throughout the load span, P is load at a given point on the load-deflection curve, L is support span, b is width of beam and d is depth of beam.

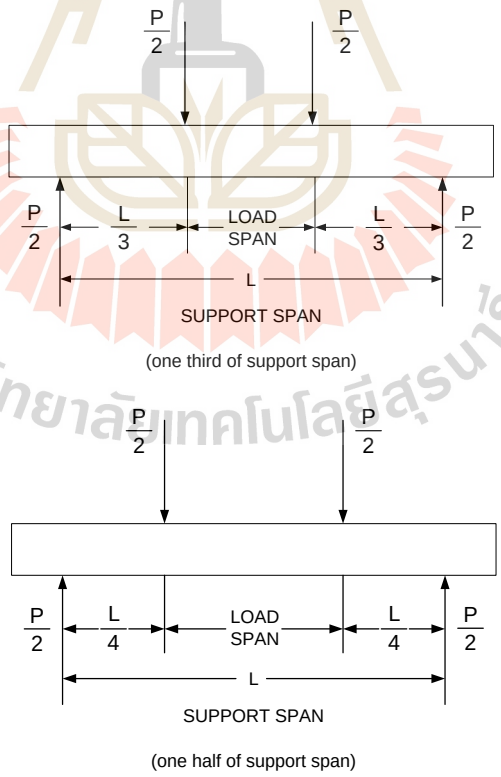

Figure 2.4 Loading Diagram (ASTM (D6272 – 02)).

The tangent modulus of elasticity is the ratio, within the elastic limit, of stress to corresponding strain and shall be expressed in megapascals (pounds per square inch). It is calculated by drawing a tangent to the steepest initial straight-line portion of the load-deflection curve and using equation (2.6) for a load span of one third the support span and equation (2.7) for a load span of one half of the support span, as follows:

$$E_B = 0.21L^3m / bd^3 \quad (2.6)$$

$$E_B = 0.17L^3m / bd^3 \quad (2.7)$$

where E_B is modulus of elasticity in bending, L is support span, B is width of beam tested, D is depth of beam tested and m is slope of the tangent to the initial straight-line.

Obert and Duvall (1967) propose the solution for the maximum stress values at the abutments for compression (bottom of beam) or tension (top of beam) (σ_{max}) as well as the maximum beam defection (δ) can be easily calculated using closed form beam equations, as follows:

$$\sigma_{max} = \gamma S^2 / 2T \quad (2.8)$$

$$\delta = \gamma S^4 / 32ET^2 \quad (2.9)$$

where E is the Young's modulus of the rock, γ is the specific weight and T is thickness.

The maximum stress at the midspan is one half of the maximum stress at the abutments. Therefore, for such a beam with fixed ends and distributed loading, yield is assumed when the maximum tensile stress in the upper part of the beam at the abutments exceeds the tensile strength of the rock. Vertical tensile fractures form at the

มหาวิทยาลัยเทคโนโลยีสุรนารี

abutments and the beam becomes simply supported (assuming no slip at the abutments) as shown in Figure 2.5(b) with a maximum tensile stress at the midspan given by

$$\sigma_{max} = 2\gamma S^2 / 3T \qquad (2.10)$$

This stress is now higher than the previous abutment stress, and therefore higher than the rock tensile strength. This leads to subsequent fracturing centered about the midspan as shown by Stimpson and Ahmed (1992). Snyder (1983) considers a laminated rock beam an excavation with a horizontal span by the normal thickness of the single layer under analysis. An elastic beam with no joints and with constant cross section a distribution of compression and tension symmetrical about the horizontal centreline of the beam is found across all plane sections within the beam as shown in Figure 2.5(a).

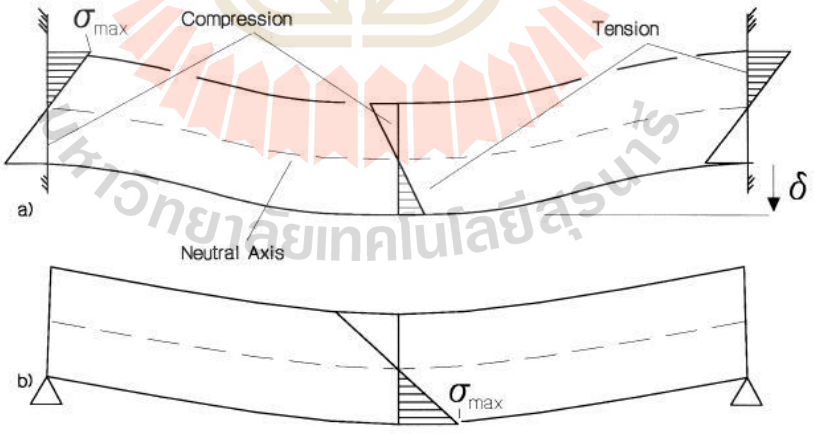

Figure 2.5 Elastic beam with (a) fixed ends and (b) simple (pin) supports. (Snyder, 1983).

Yokoyama (1988) derives a useful formulation for the stress-strain relation in a four-point bending test. His analysis utilizes the experimental measurements of the axial load, P, the strains at the top and bottom of the beam, and the geometry of the device and the beam. The derivations of Yokoyama (1988) lead to the following values of σ_t and σ_c, the maximum tensile stress and the maximum compressive stress along the beam (fiber stresses)

$$\sigma_t = [dM(\varepsilon_t + \varepsilon_c) + 2M(d\varepsilon_t + d\varepsilon_c)] / (bh^2 d\varepsilon_t) \quad (2.11)$$

$$\sigma_c = [dM(\varepsilon_t + \varepsilon_c) + 2M(d\varepsilon_t + d\varepsilon_c)] / (bh^2 d\varepsilon_c) \quad (2.12)$$

where $M = 0.5P (L_t - L_c)$ is the beanding moment of the beam (L_t and L_c are the specing of pairs of the loading point for the tensile side and for the compressive side, respesctively); ε_t and ε_c are the tensile and compressive strain measured at the top and bottom of the deformed beam, respesctively (fiber strains); b is the beam width; h is the beam hight; dM, $d\varepsilon_t$ and $d\varepsilon_c$ are the increments of the moment and the strain during the experiment (the differentials between two consecutive steps in the experiment).

2.8 Numerical method

Bauer et al. (1998) studied the roof stability of long horizontal leached caverns in bedded rock salt formations, and built a cantilever beam model to calculate the stresses in an interlayer. They thought shear and tensile failure were the main reasons causing roof stability. As shown in Figure 2.6, a 1000 psi tensile strength results in roof width to bed thickness ratios of 1 to 1.4 for 2000 and 1000 psi loads, respectively. Therefore, the bed thickness should be greater than the roof span to be stable during the

operational phase of the cavern. The bed thickness less than 70 percent of the length of the roof span are predicted to fracture near middle. When the roof bed fractures and starts to sag from the cavern roof, it will fail in tension if its thickness is less than 30 percent of its length or 15 percent of the cavern roof span.

Swift and Reddish (2001) presented to numerical modelling analysis of the current stability of the Winsford salt mine by used FLAC software to simulations of the room and pillar in rock salt. A cross section through the Bostock No. 5 panel indicating the geometry of the model is reproduced in Figure 2.7. The pillar sequence run with FLAC assumed a plane-strain situation although this is not modelling the real three-dimensional geometry. The result simulation indicate that the principal load bearing elements are the pillars. Figure 2.8 shows the maximum principal stress re-distribution around the central two rooms of the Bostock No. 5 panel and within the adjacent pillars.

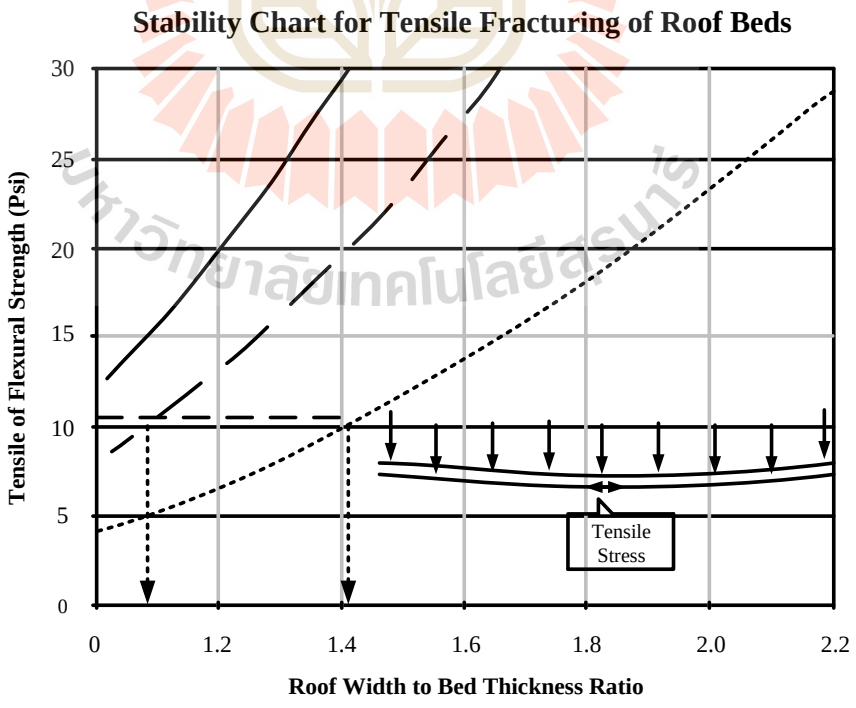

Figure 2.6 Stability chart for tensile fracturing of roof beds (Bauer et al., 1998).

The plot indicates that the redistribution of stresses is concentrated in the rock close to the mine excavation, and the influence of the excavation reduces with increasing distance from the mine voids. This plot indicates stress concentrations in the pillar centre of approximately 7 MPa, increasing to 9 MPa at the pillar abutments. The pillar core as previously defined can be clearly identified, representing the central 8 m of the pillar. The central part of the immediate roof of the room shows stress concentrations of 4 MPa. Stress concentrations increase towards the room corners, as would be expected, to a maximum of 9 MPa. Safety factors for the central pillar and adjacent rooms have been calculated as a means of illustrating the relative stability of the mine structures. Strength/stress ratios of 3 are shown in the side walls and immediate roof this would be considered to indicate very stable conditions in mining situations. However, towards the central pillar section and further in to the roof strata, the strength/stress ratio increases to in excess of 9 indicating a very stable pillar core and mine roof.

Han et al. (2006) studied the tensile failure in anhydrite layer implies an increase in the vertical displacement of the cavern roof, and thus more damage in the salt itself (see Figure 2.9). Calculation indicates that, when overburden becomes soft, the vertical displacement of the cavern roof increase to as much as 0.14 m (0.46 ft), from 0.01 m (0.0328 ft) in the baseline study. Furthermore, the interface slippage between the salt layer and the anhydrite layer now covers the entire cross section of cavern. This simulation clearly demonstrates that the overburden stiffness is a significant factor in evaluating roof stability of caverns.

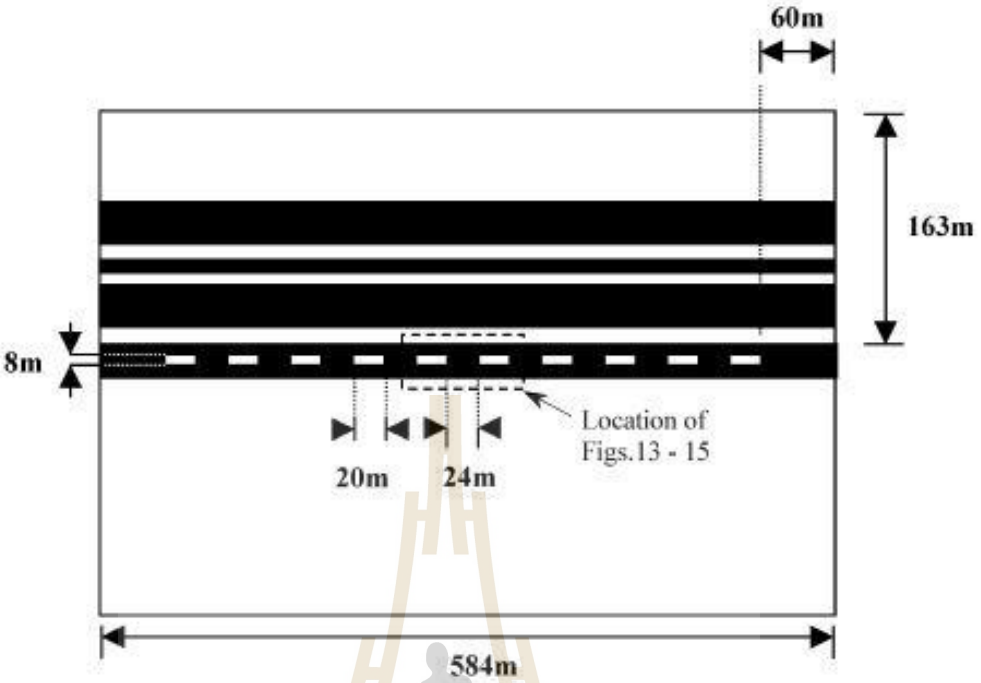

Figure 2.7 Cross section through the Bostock No. 5 panel showing model configuration (Swift and Reddish, 2001).

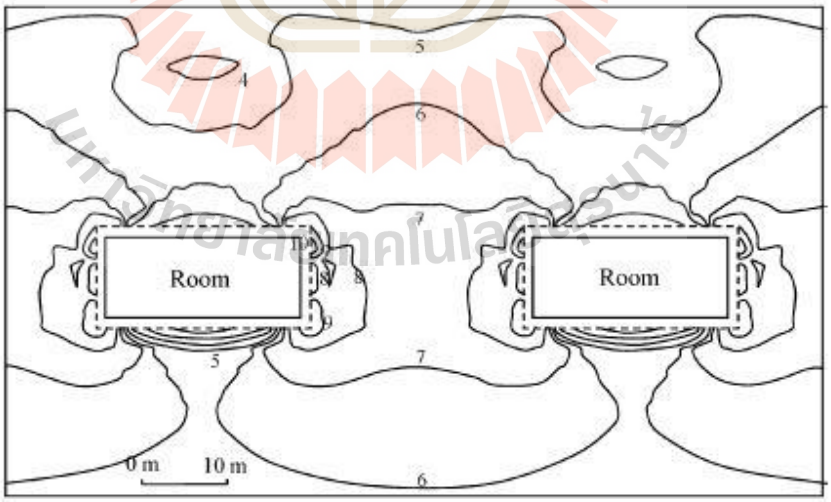

Figure 2.8 Maximum principal stress distribution around central two rooms in the Bostock No. 5 panel (in MPa) (Swift and Reddish, 2001).

Wang et al. (2012) build up the numerical simulation model. According to the cavern dimensions and properties of rock salt and non-salt, the 3D numerical model of bedded rock salt cavern gas storage is established by FLAC 3D software. The results show that buried depth, roof span and gas pressure have significant effects on the roof stability and can be controlled in the designs and operations. Therefore, the proper buried depth, strictly designed cavern roof and short time of low gas pressure are recommended in the design of bedded rock salt cavern gas storage. As the stiffness and strength of non-salt are usually very low, a relative thick roof salt is recommended to maintain the cavern roof stability.

Wang et al. (2015) improved calculation efficiency by used to FLAC 3D for the model symmetry. The model dimensions are 900 x 800 x 400 m in length, height, and width, respectively. The target of rock salt formation is located with depth from 1900 m to 2098 m. The thickness of top and bottom mudstone layers are about 300 m. The bottom of the model has zero displacement boundary. The relative horizontal and vertical displacements of the bottom are all zero. The left and right sides of the model both have zero horizontal displacement boundaries.

Yang et al. (2016) studied mechanical theory of the roof interbed in terms of land subsidence brought by brine in salt cavity after removal, and also they listed some possible failures of the interbed such as tension failure, shear failure, crushing failure, and plastic yield. Then, roof peel, tension failure and maximum deflection were obtained by FLAC software, but this study did not explain the detailed mechanical theory for kinds of failure, and the influence of horizontal stress on roof collapse also could not be introduced in their study.

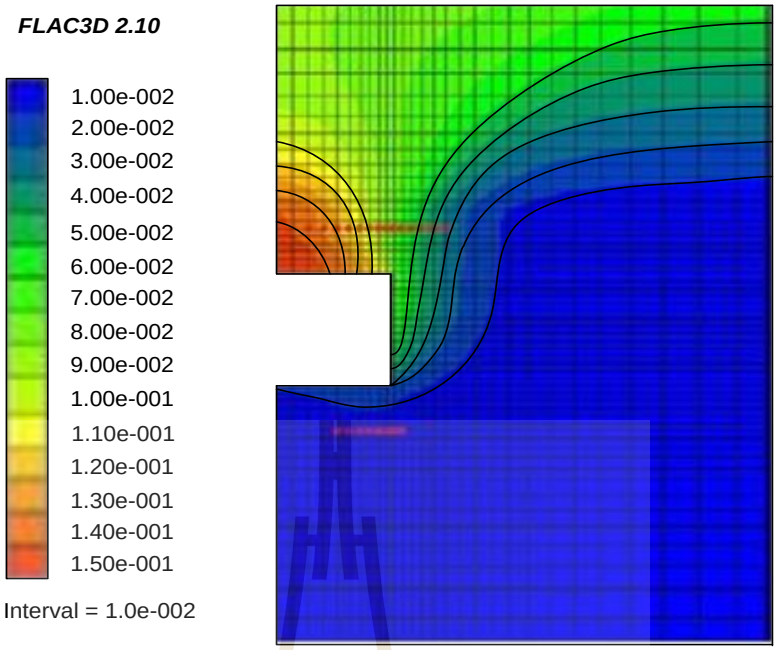

Figure 2.9 Rock displacement around a cavern with reduced overburden stiffness **(**Han et al., 2006).

มหาวิทยาลัยเทคโนโลยีสุรนารี

CHAPTER III

SAMPLE PREPARATION

3.1 Introduction

This chapter describes the procedure and methods of preparation for rock specimen in the laboratory. The rock specimen used in the test is rock salt with various carnallite contents ranging from 0 to 95%. The tested samples have been obtained from underground openings in the northeast of Thailand (Figure 3.1).

3.2 Sample preparation

The tested samples have been obtained from underground openings of ASEAN Potash Mining Co., Ltd. (APMC). They belong to the Lower Salt member of the Maha Sarakham formation. Warren (1999) describes the origin and geological structures of the Maha Sarakham salt. The samples mainly contain inter-beds of halite and carnallite. They are sometimes called carnallitite. The specimens used for four-point bending tests are prepared as prismatic blocks with nominal dimensions of 50×50×200 mm. Figure 3.2 shows examples of the specimens with different carnallite contents. Chemical analyses by X-ray diffraction (XRD) performed on some specimens show that the primary chemical compositions of the specimens are halite and carnallite, which are of interest in this study (Table 3.1). Due to the difference of densities between halite and carnallite, the carnallite contents ($C_{\%}$) for each specimen can be determined by the following relation:

$$C_{\%} = [(\rho_s - \rho) / (\rho_s - \rho_c)] \times 100 \quad (3.1)$$

where ρ is density of the specimen, ρ_s is density of halite (2.16 g/cc) and ρ_c is density of carnallite (1.60 g/cc) (Klein et.al., 1998). Table 3.2 show specimen dimensions prepared for four-point bending testing.

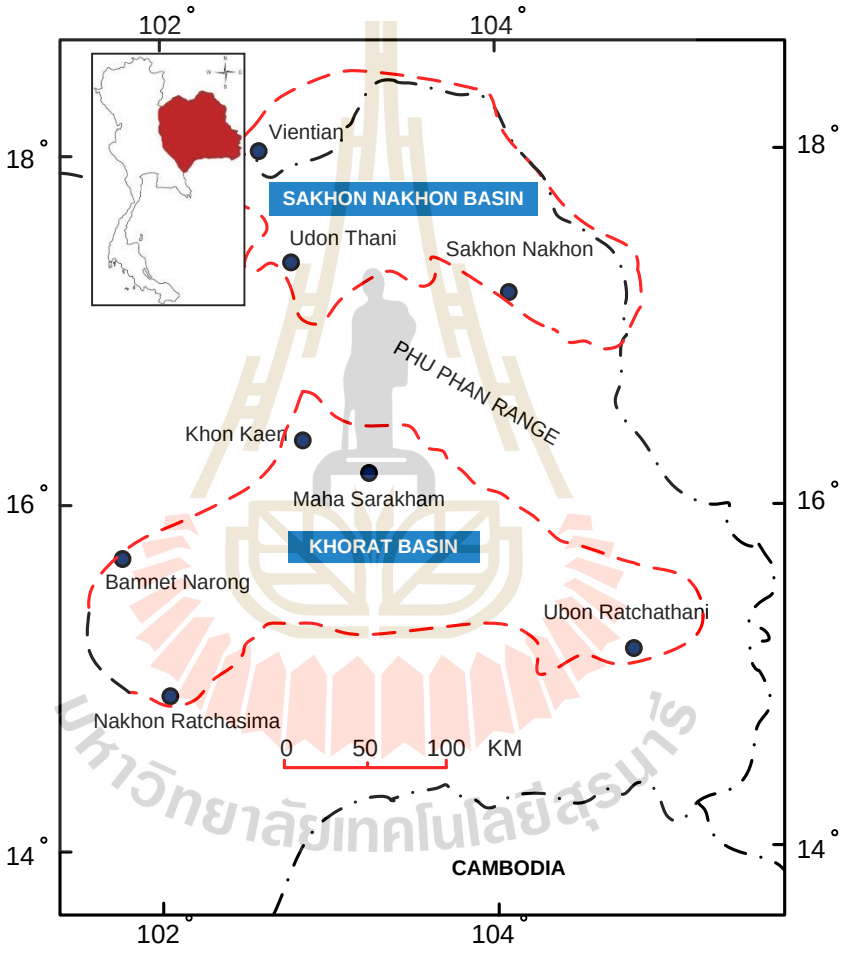

Figure 3.1 The source of rock samples used in the testing (Suwanich, 2007).

Table 3.1 Chemical compositions of some specimens.

Components	**Sample (1)**	**Sample (2)**	**Sample (3)**	**Sample (4)**
Carnallite ($KMgCl_3$ $6H_2O$)	0.05	24.75	38.31	52.98
Halite (NaCl)	92.4	64.6	42.8	35.97
$MgCl_2$	5.71	8.93	9.69	5.55
Calcite ($CaCO_3$)	0	0.21	0.48	1.92
Anhydrite ($CaSO_4$)	0.11	0.17	0.65	1.23
Sylvite (KCl)	0.09	0.19	6.1	1.01
Hydrophilite ($CaCl_2$)	0	0	1.64	0.56
Wuestite	0	0.06	0.43	0.44
Calcium Chloride (CaCl)	1.65	1.08	0.89	0.33
Density (g/cc)	2.11	1.96	1.89	1.76
$C_{\%}$ (determined by density ratio)	8.56	36.12	49.01	71.08

3.2 Strain gage installation

A strain gage (TML, PFL-20-11-1L, 20 mm) is installed to measure tensile strains at the center of the specimen in horizontal and the main axis of the specimen is parallel to the bedding planes (Figure 3.3). Gage length is 20 mm. Gage factor is 2.13±1%.

มหาวิทยาลัยเทคโนโลยีสุรนารี

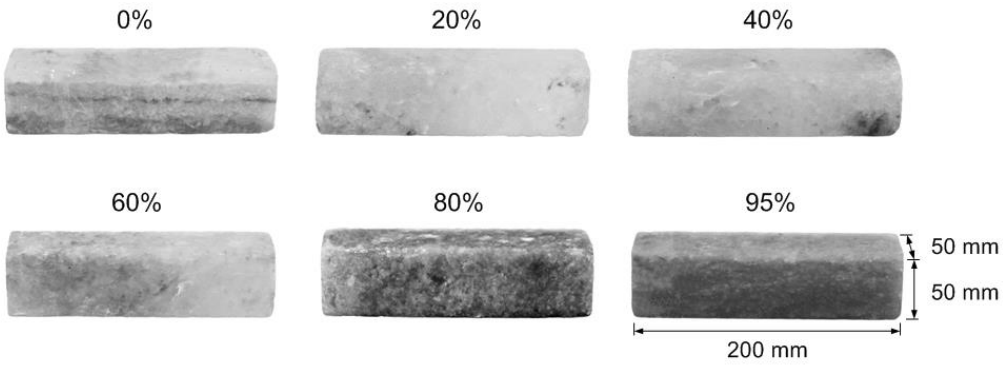

Figure 3.2 The rock samples used in the testing various carnallite content.

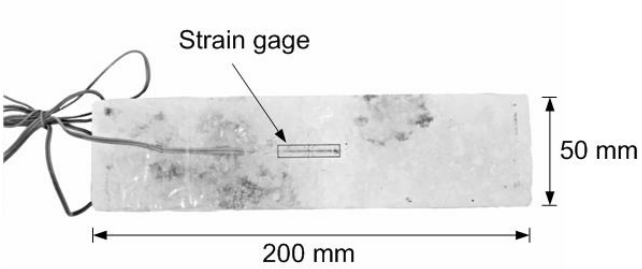

Figure 3.3 Examples of prismatic specimens with strain gage position

Table 3.2 Specimen dimensions prepared for four-point bending testing.

Specimen No.	Length (mm)	Width (mm)	Height (mm)	Density (g/cc)	$C_{\%}$ (%)
PT-04	200.08	49.70	51.10	1.62	91.00
PT-17	198.82	51.58	50.84	1.67	86.72
PT-20	200.58	48.75	49.72	1.80	65.00
PT-22	199.68	51.43	49.88	1.83	58.68
PT-26	199.11	49.83	50.14	1.85	55.54
PT-27	200.78	50.02	50.55	1.62	95.34
PT-29	199.78	50.65	50.57	2.01	26.78
PT-30	195.36	48.58	48.95	1.74	74.87
PT-31	201.78	50.12	50.25	2.16	0.00
PT-32	203.04	50.42	50.23	1.65	91.07
PT-33	201.75	50.58	50.52	1.82	61.49
PT-34	201.86	50.21	48.65	1.64	92.37
PT-37	202.05	49.60	48.64	2.06	17.33
PT-39	199.93	50.00	50.82	2.02	24.68
PT-42	202.30	50.98	51.25	1.89	47.36
PT-45	202.93	52.03	50.75	1.98	32.14
PT-46	201.10	51.88	51.63	1.94	40.11
PT-48	200.53	51.53	51.68	1.92	42.39

Table 3.2 Specimen dimensions prepared for four-point bending testing (con.).

Specimen No.	Length (mm)	Width (mm)	Height (mm)	Density (g/cc)	$C_{\%}$ (%)
PT-50	202.68	50.83	51.48	1.99	30.86
PT-51	200.96	50.61	51.63	2.05	19.64
PT-54	197.44	49.85	47.87	1.74	75.53
PT-64	201.06	49.00	44.44	2.11	0.00
PT-66	194.38	50.15	50.50	2.10	0.00
PT-67	205.05	50.01	50.50	2.08	0.00

มหาวิทยาลัยเทคโนโลยีสุรนารี

CHAPTER IV

LABORATORY TESTING

AND TESTING RESULTS

4.1 Introduction

The objective for four-point bending test is to determine the maximum tensile stress of rock salt. The results of the test can be applied to assess the stability of underground mine roof due to that the stress distribution on rock specimen is similar to the stress distribution in the roof layer. The tensile strength values obtained from four-point bending test are conservative for the roof stability assessment. This chapter describes the test methods and results of the tensile strength of the Maha Sarakham salt under various carnallite contents and loading rates. The testing procedures and equipment are also described.

4.2 Test method

The test configurations follow the ASTM (D6272-02). Figure 4.1 shows the positions of the loading for the upper and lower bearing plates. A data logger (TC-32K) connected with the switching box (Type B-2760) is used to monitor the induced tensile strains (Figure 4.2). The loads are applied under four constant rates from 0.045 N/s to 45 N/s, which are equivalent to the induced tensile stress rates at the center of the specimen from 10^{-6} to 10^{-3} MPa/s. The load is applied until failure occurs.

The post-failure characteristics are observed and recorded. The induced tensile stress is calculated by:

$$\sigma_t = PL / bd^2 \quad (4.1)$$

where σ_t is tensile stresses, P is the applied load, L is support span (180 mm), b is specimen width (50 mm), and d is specimen thickness (50 mm). The tensile stress is defined here as positive values for a convenience of presentation.

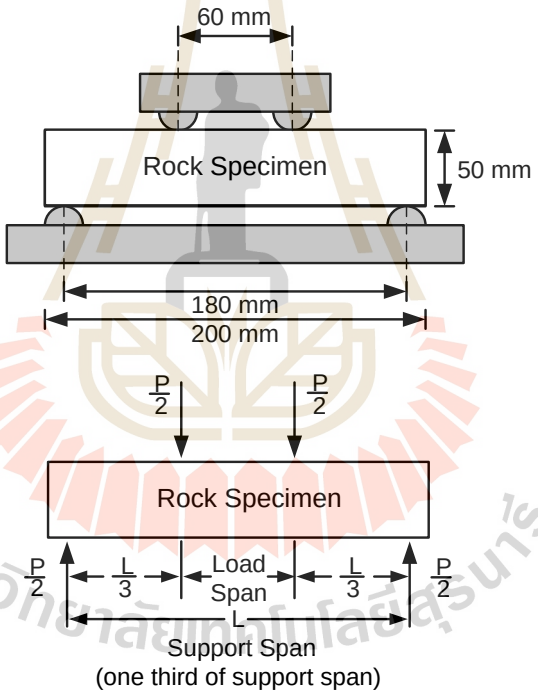

Figure 4.1 Test arrangement for four-point bending test (ASTM (D6272 – 02)).

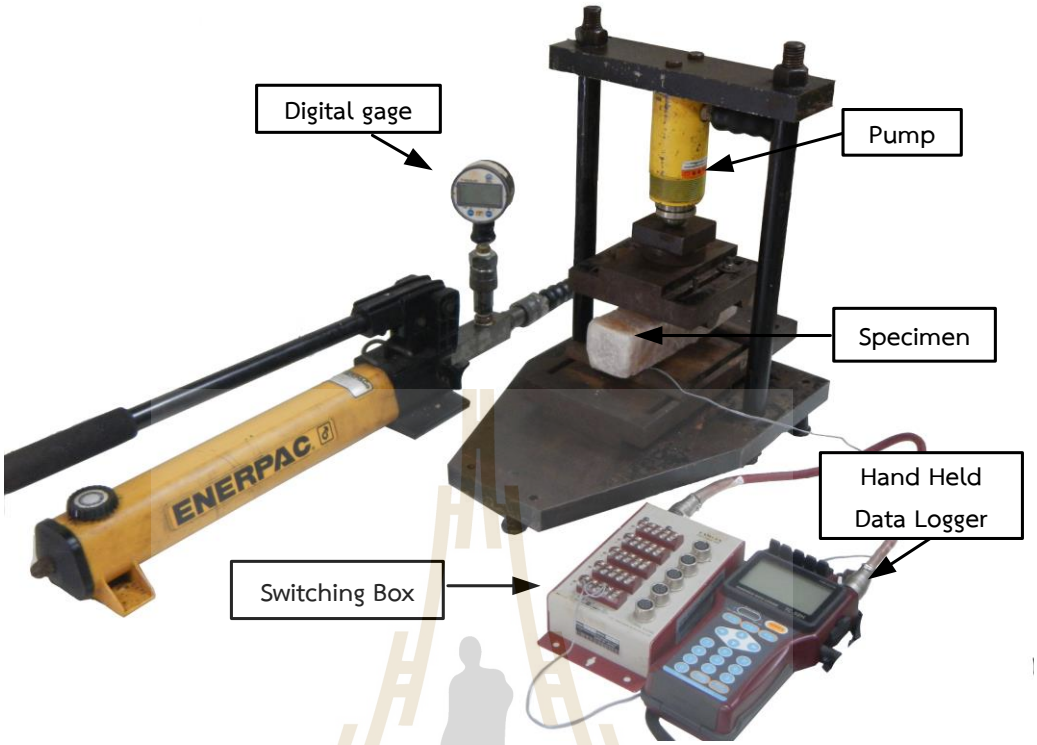

Figure 4.2 Four-point bending test.

4.3 Test results

Figure 4.3 shows some post-test specimens of the Maha Sarakham salt obtained from four-point bending testing under various carnallite contents and loading rates. Table 4.1 summarizes the test results. Post-failure observations show that there were two types of fracturing found in the rock salt specimens: cleavage fracturing (splitting of salt crystals at the cleavages) and inter-granular fracturing and the failure zone located within load span. The salt tensile strengths are plotted as a function of stress rate under various carnallite contents (Figure 4.4). Figure 4.5 shows example the stress-strain curves of some salt specimens. The test results indicate that tensile strengths decrease when the carnallite contents increase and tensile strength increases with increasing loading rates and tensile strains decreases with increasing loading rates,

which agrees with the experimental observations by Wisetsaen et al. (2015) as shown in Figure 4.6. Figures above shows the specimens tend to non-linear behavior, particularly under carnallite contents ranging from 0-60% with low loading rates and carnallite contents higher than 60% the specimens tend to behavior is linear, Obviously when higher loading rates.

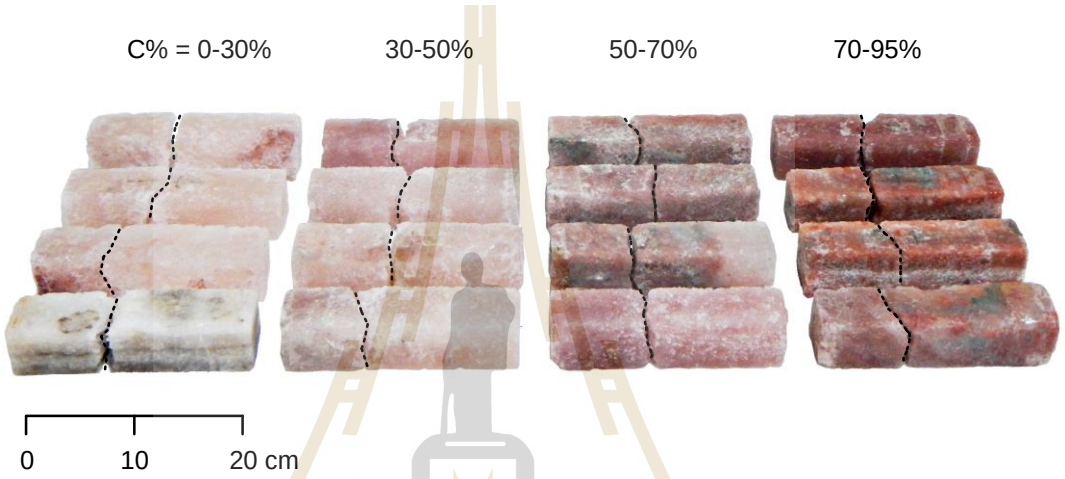

Figure 4.3 Some post-test specimens of the Maha Sarakham salt obtained from four point bending testing under various carnallite contents and loading rates.

มหาวิทยาลัยเทคโนโลยีสุรนารี

Table 4.1 Test results of four-point bending test.

$\partial\sigma/\partial t$ (MPa/s)	$C_{\%}$ (%)	σ (MPa)	ε (milli-strains)	Time (sec)
0.004	0	3.21	0.99	510
	20	2.15	0.87	380
	32	1.69	0.76	320
	47	1.25	0.68	210
	65	0.88	0.57	140
	91	0.52	0.53	60
0.0004	0	2.17	1.73	6870
	17	1.55	1.62	3150
	40	0.98	1.38	2310
	56	0.71	1.21	1500
	87	0.38	1.09	1080
	93	0.34	1.06	540
0.00004	0	1.47	1.90	22800
	25	0.89	1.66	16000
	42	0.63	1.55	10800
	62	0.42	1.32	7000
	76	0.32	1.32	3200
	95	0.22	0.82	2400
0.000004	0	0.99	2.24	73800
	27	0.58	2.04	55800
	31	0.53	1.81	38700
	59	0.3	1.54	20700
	75	0.22	1.34	14400
	92	0.16	1.10	8100

มหาวิทยาลัยเทคโนโลยีสุรนารี

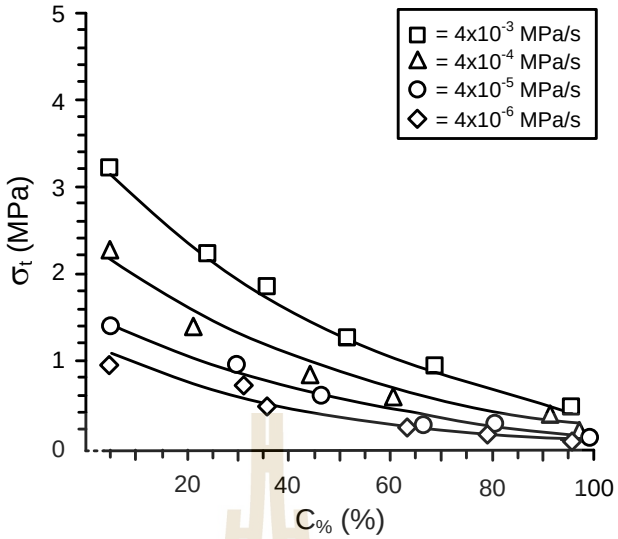

Figure 4.4 Tensile strength as a function of carnallite contents.

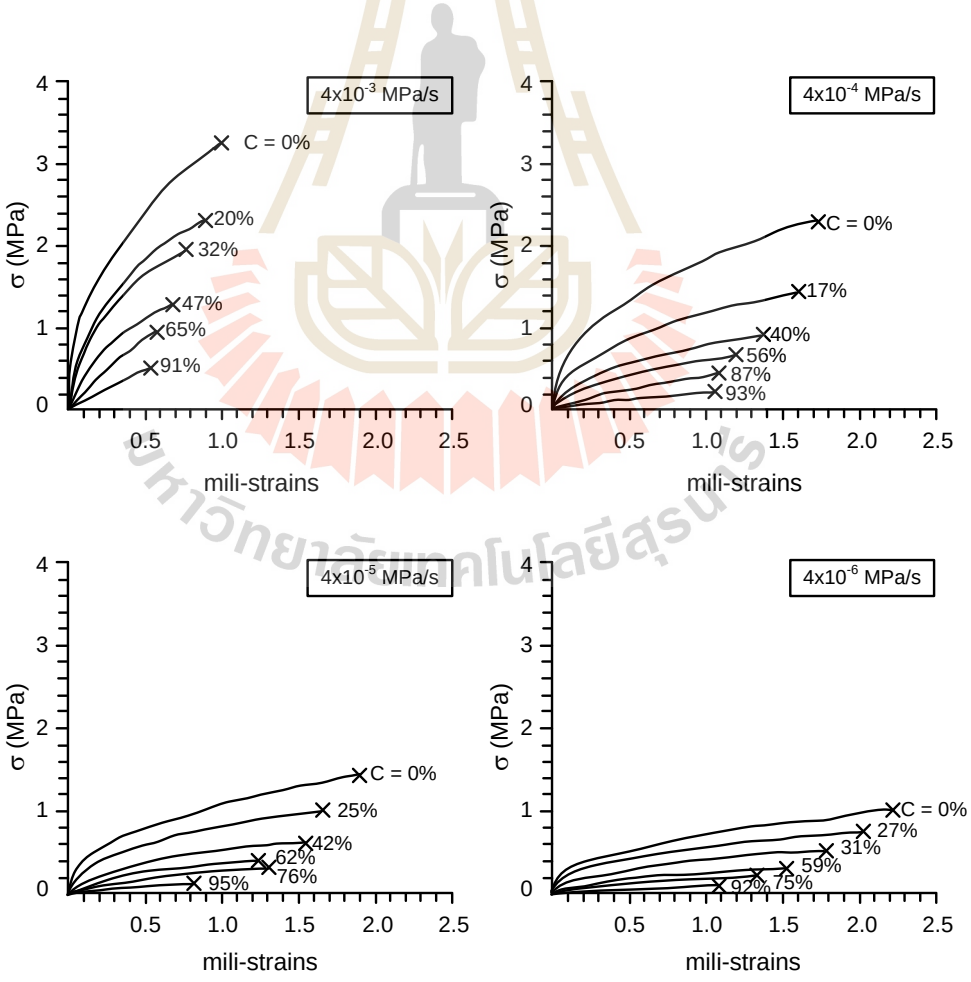

Figure 4.5 Tensile stress-strain curves for various loading rates.

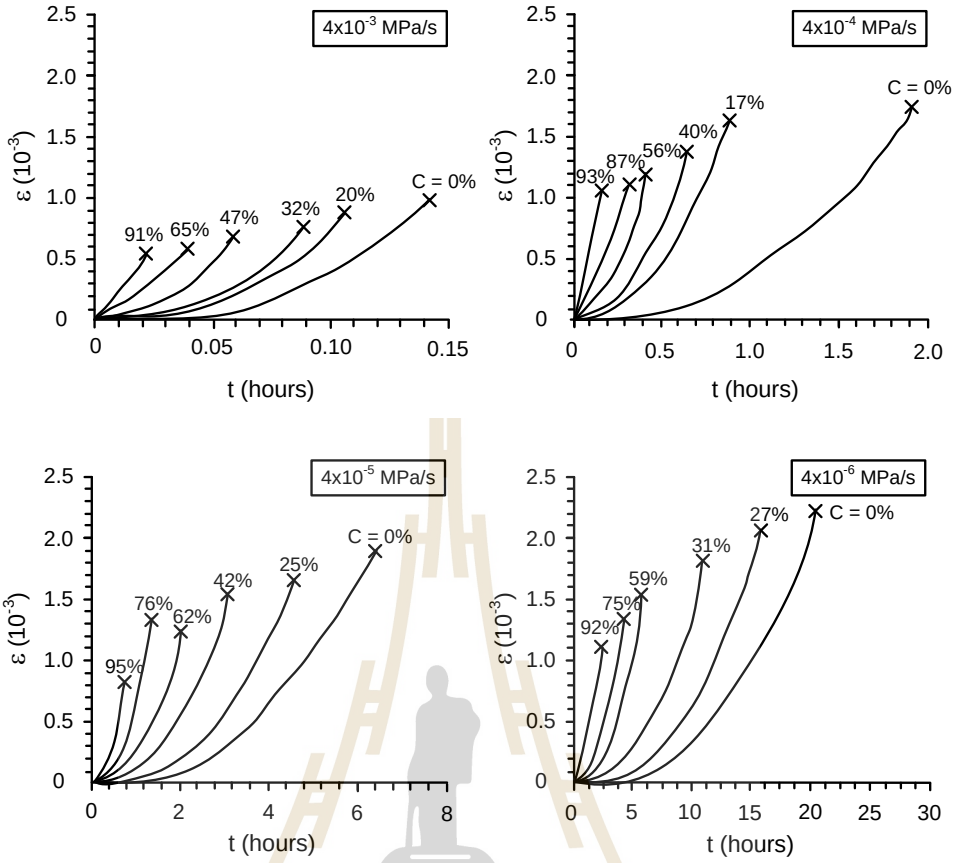

Figure 4.6 Tensile strain-time curves for various loading rates.

มหาวิทยาลัยเทคโนโลยีสุรนารี

CHAPTER V

SALT PROPERTIES CALIBRATION AND STRENGTH CRITERION

5.1 Introduction

The purpose of this chapter is to describe the calibration results for the elastic and viscosity parameters. The regression analysis on the linear visco-elastic equation of the Maxwell model is employed in the calibration. The data used in the calibration are obtained from the four-point bending tests. Results from the laboratory measurements in terms of the tensile strength of rock salt under various carnallite contents and loading rates are also be used to formulate mathematical relations. For an ease of result presentation, the tensile stress is defined as positive values.

5.2 Maxwell model

The Maxwell model is used here to describe the time-dependent deformation of the specimens under different stress rates. Its elastic and viscosity parameters can be derived from the test results, and hence the series of tensile strain-time curves can be constructed for various applied tensile stresses. Figure 5.1 shows the physical components arranged in the Maxwell model. It is postulated here that under tensile stress and unconfined condition the salt would exhibit the instantaneous (elastic) deformation and plastic flow due to the dislocation climb mechanism (sliding between

grains). The governing equation for constant stress rate can present the tensile strain as a function of time as follows (Fuenkajorn and Daemen, 1988):

$$\varepsilon_t = \sigma_R [(t / E) + (t^2 / 2\eta)] \quad (5.1)$$

where ε_t is tensile strain, σ_R is constant stress rate, t is elapse time, E is elastic parameter, η is viscosity parameter.

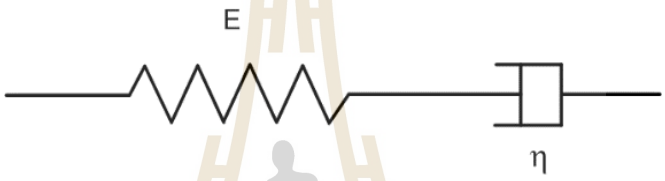

Figure 5.1 Modular components of Maxwell model (Fuenkajorn and Daemen, 1988).

Regression analyses are performed on the strain-time data using the SPSS statistical software (Wendai, 2000) to determine the Maxwell parameters for each salt specimen. Table 5.1 shows the elastic and viscosity parameters of the Maxwell model calibrated from four-point bending tests.

มหาวิทยาลัยเทคโนโลยีสุรนารี

Table 5.1 Maxwell parameters calibrated from the four-point bending tests.

$\partial\sigma/\partial\tau$ (MPa/s)	**$C_{\%}$ (%)**	**E (GPa)**	**η (GPa.day)**
0.004	0	4.43	0.056
	20	4.59	0.059
	32	4.66	0.060
	47	4.73	0.061
	65	4.79	0.062
	91	4.84	0.063
0.0004	0	4.59	0.059
	17	4.68	0.060
	40	4.77	0.062
	56	4.81	0.062
	87	4.86	0.063
	93	4.87	0.063
0.00004	0	4.69	0.060
	25	4.78	0.062
	42	4.82	0.062
	62	4.86	0.063
	76	4.87	0.063
	95	4.89	0.063
0.000004	0	4.77	0.062
	27	4.83	0.063
	31	4.84	0.063
	59	4.88	0.063
	75	4.89	0.063
	92	4.9	0.064

มหาวิทยาลัยเทคโนโลยีสุรนารี

The results show that the elastic and viscosity parameters decrease exponentially with the carnallite contents, as shown in Figures 5.2 and 5.3. It could be explained by the complex mechanical responses of the two different materials are halite and carnallite within the specimen. When the carnallite contents are toward 100% the specimens tend to behave as viscous material with very low elastic parameter which can be best represented by an empirical equation:

$$E = \delta \cdot \exp(-\delta' \cdot C_{\%}) \quad \text{(GPa)} \tag{5.2}$$

$$\eta = \omega \cdot \exp(-\omega' \cdot C_{\%}) \quad \text{(GPa)} \tag{5.3}$$

where $C_{\%}$ is carnallite contents, δ, δ', ω and ω' are empirical constants, equals to 4.93 GPa, 0.03, 0.06 GPa·day, 0.04, respectively.

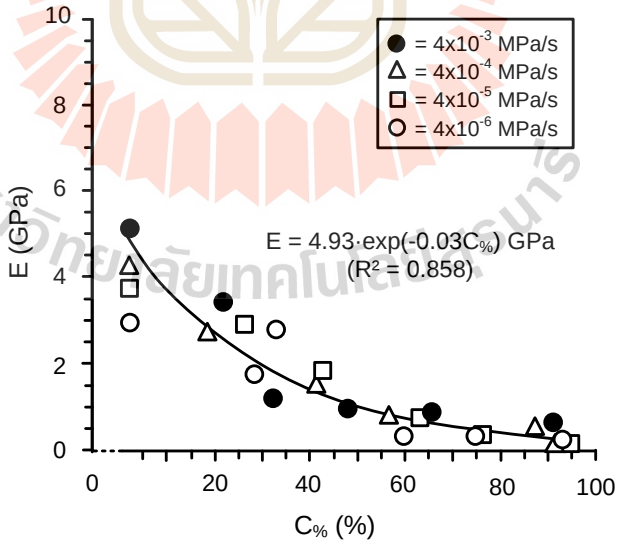

Figure 5.2 Elastic parameters of Maxwell model plotted as a function of $C_{\%}$.

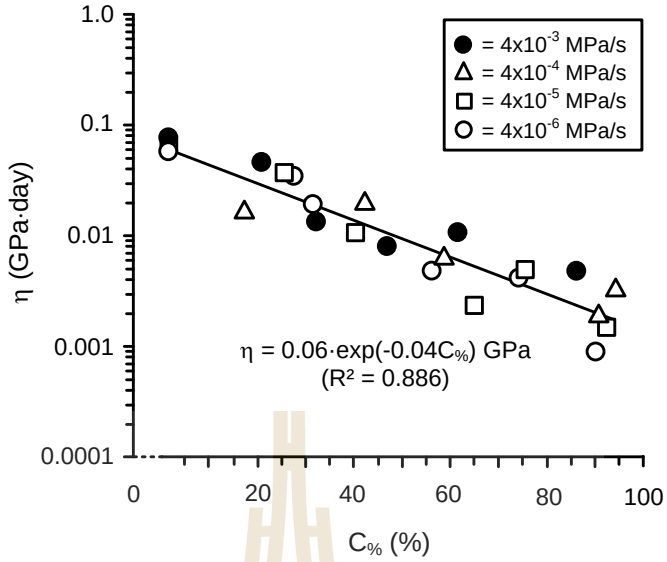

Figure 5.3 Viscosity parameters of Maxwell model plotted as a function of $C_{\%}$.

5.3 Strength criterion

5.3.1 Tensile strength as a function of carnallite contents and stress rate

The tensile strengths are plotted as a function of carnallite contents and stress rates, as shown in Figures 5.4 and 5.5. The results indicate that the tensile strengths decrease with increasing carnallite contents. The strength reduction under different stress rates ($\partial\sigma/\partial t$) can be represented by an exponential equation:

$$\sigma_t = \alpha \cdot \exp(-\alpha' \cdot C_{\%}) \cdot \partial\sigma/\partial t^{\chi} \quad \text{(MPa)} \qquad (5.4)$$

where α, α' and χ are empirical constants, equals to 8.21 MPa, 0.02, 0.17, respectively.

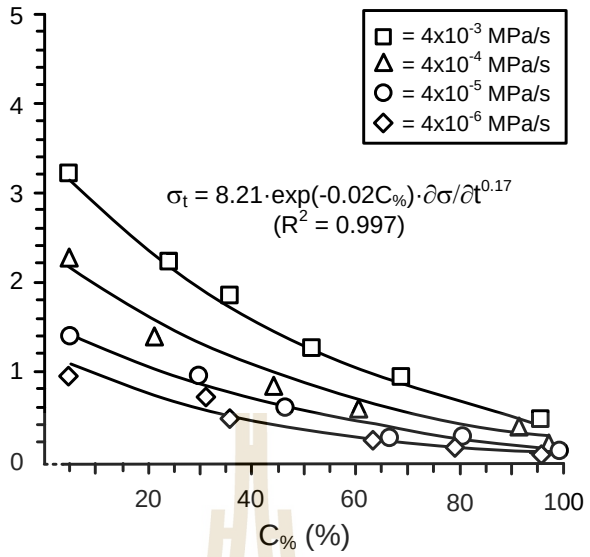

Figure 5.4 Tensile strength as a function of carnallite contents.

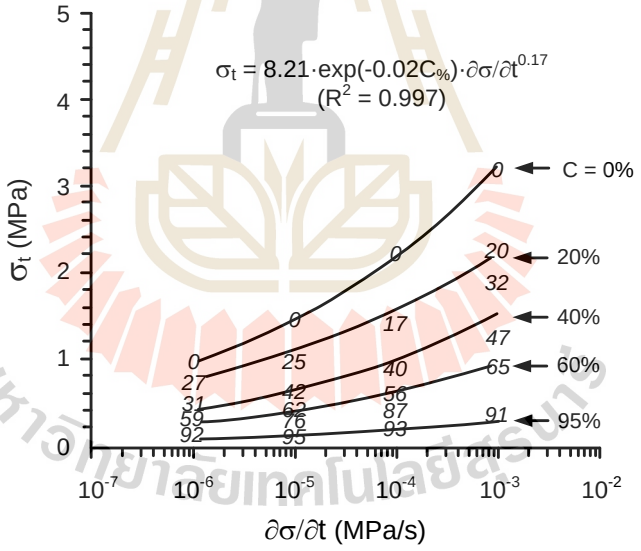

Figure 5.5 Tensile strength as a function of stress rate.

5.3.2 Strain energy criterion

The strain energy principle is applied here to describe the specimen strengths and deformability with different carnallite contents and loading rates. The strain energy density can be calculated by (Jaeger et al., 2007):

$$W = ½ (\sigma_1\varepsilon_1 + \sigma_2\varepsilon_2 + \sigma_3\varepsilon_3) \quad (5.5)$$

For one-dimensional W is reduced to:

$$W = ½ (\sigma_1\varepsilon_1) \quad (5.6)$$

where $\varepsilon_1, \varepsilon_2, \varepsilon_3$ are principal strain and $\sigma_1, \sigma_2, \sigma_3$ are principal stresses

$$W = ½ (\sigma_T\varepsilon_T) \quad (5.7)$$

where ε_T is strain and σ_T is stress

Figure 5.6 shows the results while they are plotted as a function of carnallite contents. The results indicate that the strain energy of the tested specimens decreases exponentially with increasing carnallite contents. The empirical equations can be written as:

$$W_t = \lambda \cdot \exp(-\kappa \cdot C_{\%}) \quad \text{(kPa)} \quad (5.8)$$

where λ and κ are empirical constants, equals to 2.17 kPa and 0.03, respectively.

The above equation implies that the specimens with carnallite contents toward 100% cannot sustain the potential energy caused by the applied tensile stress and

induced strain. If the carnallite content is known, its strength can be determined from equation (5.7) regardless the loading rate. The derived criteria will be used to evaluate the mine roof stability to be presented in the following chapter. Table 5.2 summarizes these stress, strain energy, carnallite contents and loading rates of all specimens.

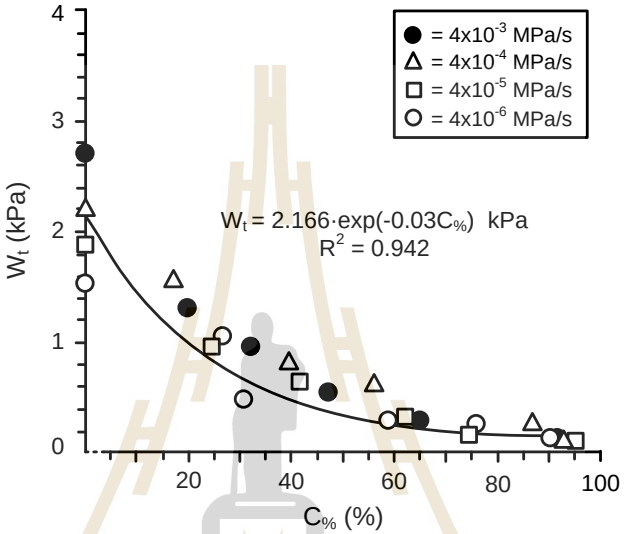

Figure 5.6 Strain energy density as a function of $C_{\%}$.

มหาวิทยาลัยเทคโนโลยีสุรนารี

Table 5.2 Summarizes stress, spring constant and viscosity parameters and strain energy.

$\partial\sigma/\partial t$ (MPa/s)	$C_{\%}$ (%)	σ_T (MPa)	ε_T (milli-strains)	W (kPa)
$4x10^{-3}$	0	3.21	0.99	2.18
	20	2.15	0.87	1.33
	32	1.69	0.76	0.98
	47	1.25	0.68	0.55
	65	0.88	0.57	0.29
	91	0.52	0.53	0.15
$4x10^{-4}$	0	2.17	1.73	2.30
	17	1.55	1.62	1.56
	40	0.98	1.38	0.82
	56	0.71	1.21	0.64
	87	0.38	1.09	0.27
	93	0.34	1.06	0.11
$4x10^{-5}$	0	1.47	1.90	1.86
	25	0.89	1.66	1.00
	42	0.63	1.55	0.67
	62	0.42	1.32	0.34
	76	0.32	1.32	0.28
	95	0.22	0.82	0.10
$4x10^{-6}$	0	0.99	2.24	1.78
	27	0.58	2.04	1.07
	31	0.53	1.81	0.51
	59	0.30	1.54	0.30
	75	0.22	1.34	0.20
	92	0.16	1.10	0.13

มหาวิทยาลัยเทคโนโลยีสุรนารี

CHAPTER VI

NUMERICAL MODELLING

6.1 Introduction

This chapter describes the method and results of finite difference analysis by using FLAC (Itasca, 1992) to simulate of the mine roof in rock salt. The simulations to study tensile stress and tensile strain at occur in mine roof can be used predicted standup time of mine roof will be presented in the next chapter.

6.2 Numerical modelling (FLAC program)

The finite difference code FLAC 4.0 is used in the simulations because it can describe for the time-dependent deformation of the mine roof in two dimensional domain. The simulation determines the maximum tensile stresses in mine roof for $C_{\%}$ from 0%, 20%, 40%, 60%, 80% to 100%, and room widths from 8, 10 to 12 m. The pillar width and room high are 20 and 6 m, respectively. The roof thickness is defined as 40% of the room width to comply with the local regulations. The opening depths are 230, 270 and 320 m. The overburden and underlying rocks are inter-bedded of the rock salt group are the upper clastics, upper salt, middle clastics, middle salt, and lower salt beds. The analysis is made in plane strain condition. Finite difference mesh of mine roof use the mesh consists of 2000 elements covering an area of simulation. The left and right boundaries are fixed in the x-axis, and the bottom boundary is fixed in the y-axis. The top boundary can move freely in both directions. The simulation

are made up to 50 years after excavations. The finite difference mesh for the simulation and model stratigraphic units from Asia Pacific Potash Corporation, as shown in Figures 6.1 to 6.3.

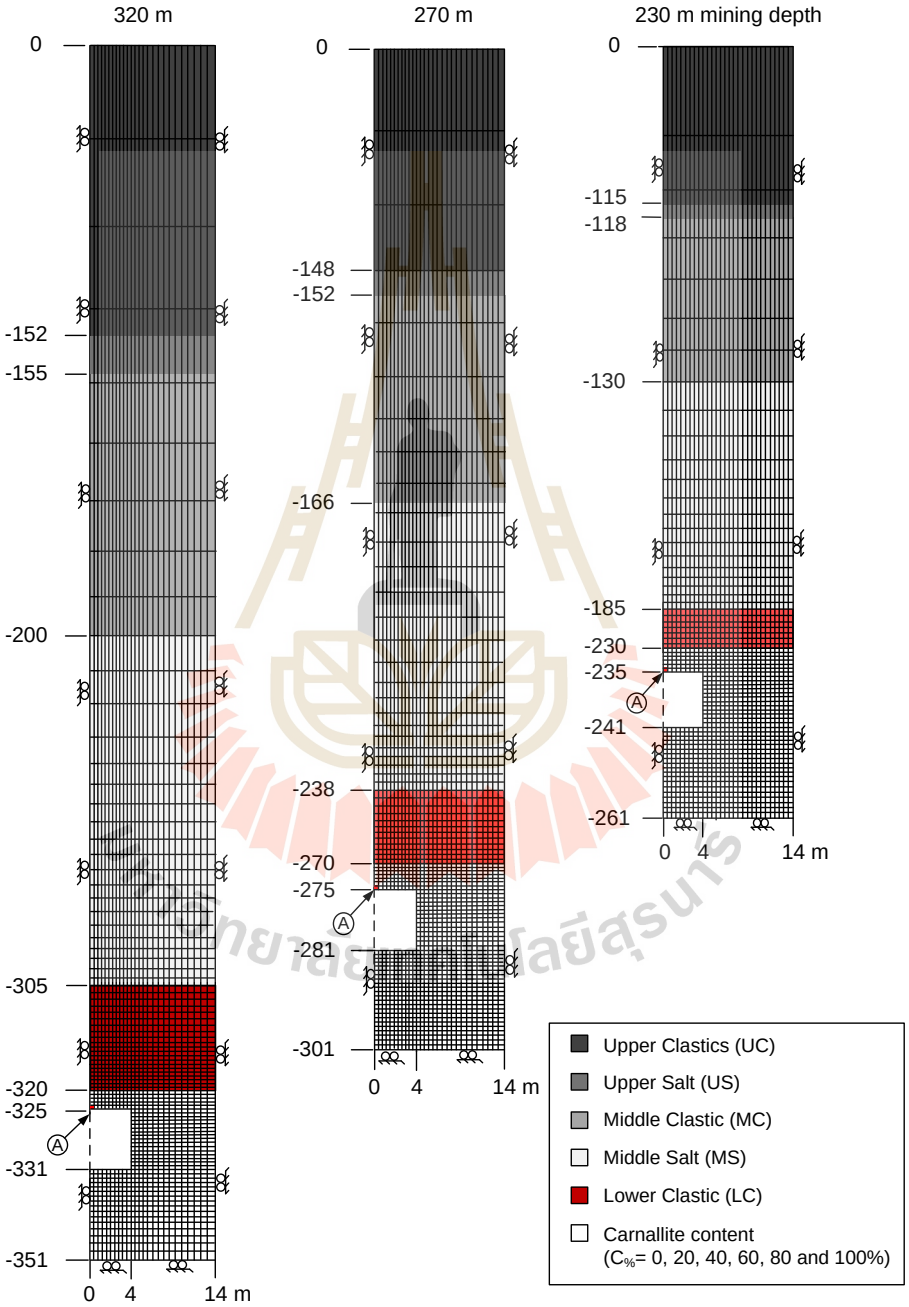

Figure 6.1 Finite difference mesh developed for FLAC simulation, mining depths are 230, 270 and 320 m and room width is 8 m.

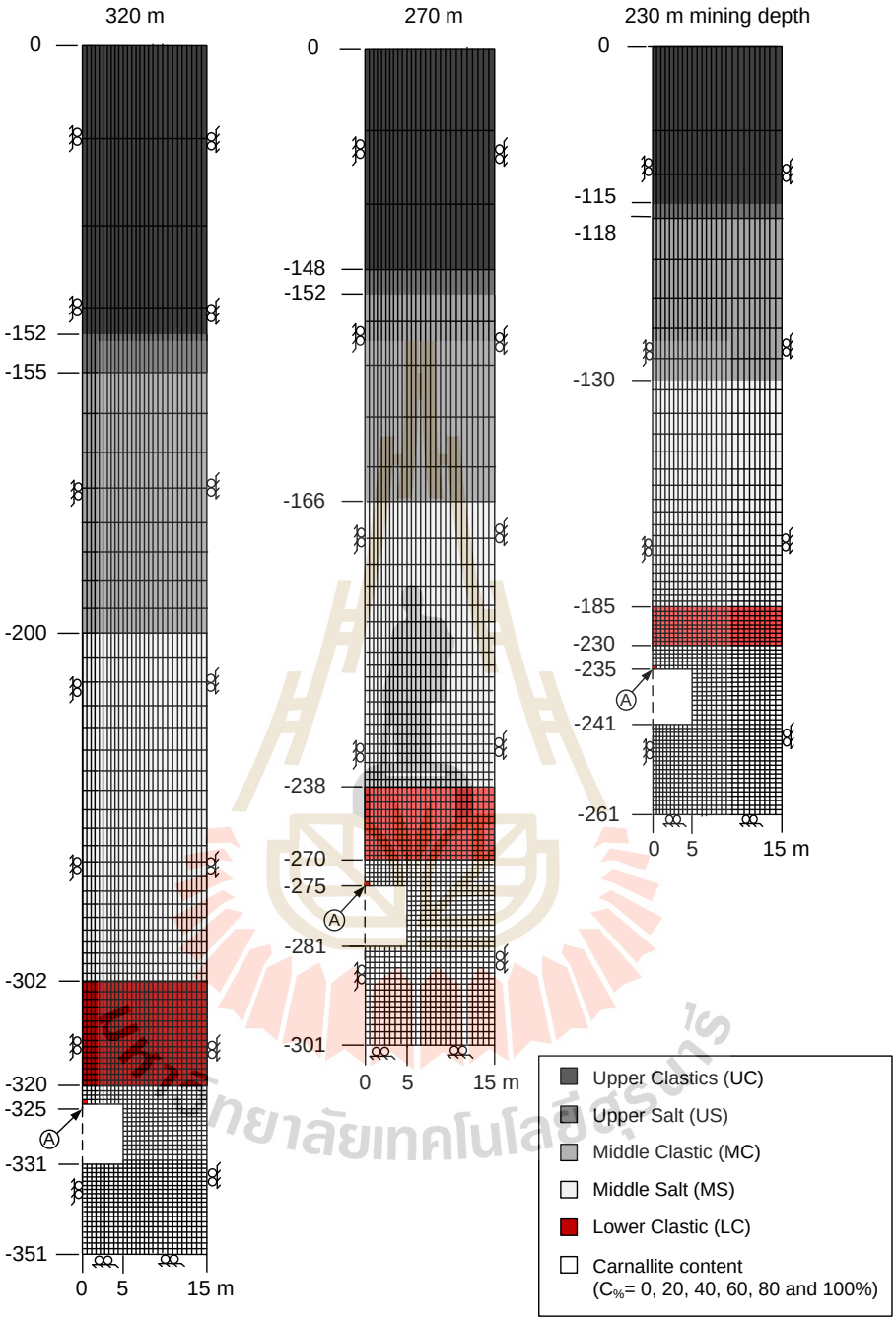

Figure 6.2 Finite difference mesh developed for FLAC simulation, mining depths are 230, 270 and 320 m and room width is 10 m.

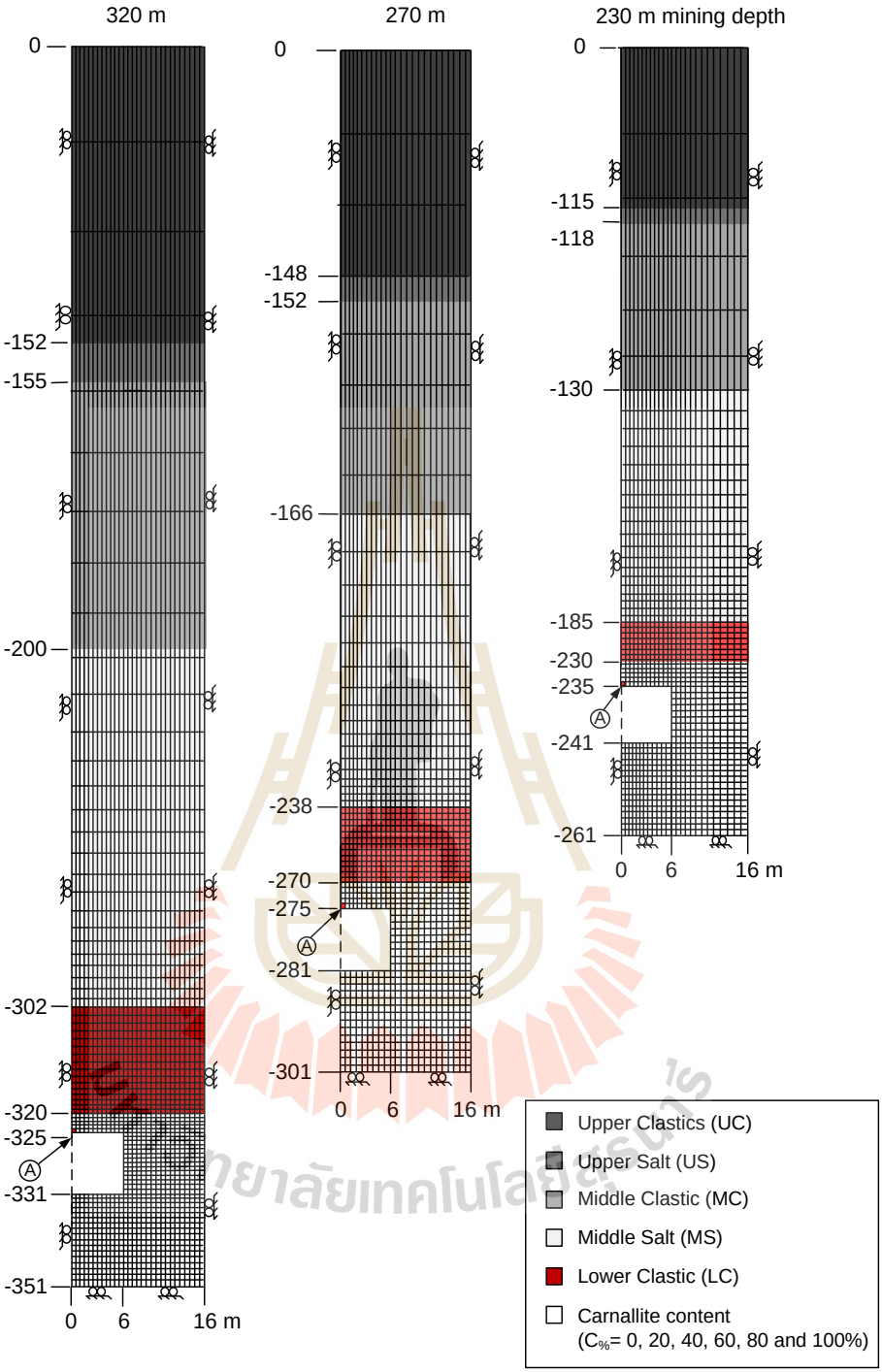

Figure 6.3 Finite difference mesh developed for FLAC simulation, mining depths are 230, 270 and 320 m and room width is 12 m.

6.3 Property parameters used in numerical modelling

Table 6.1 shows the material parameters used for numerical modeling (Crosby (2005) and Luangthip et al. (2016)). The overburden formations are assumed to be elastic and gives material properties of the Lower Salt member: rock salt with various carnallite contents ranging from 0%, 20%, 40%, 60%, 80% to 100%. The Lower Salt member is assumed to behave as the Burgers material. The Burgers parameters are obtained from the calibration results of creep test by Wilalak and Fuenkajorn (2016). These parameters are given in Table 6.2. They are incorporated into the built-in FLAC subroutine to compute the changes of stress and strain with time for the roof beam.

Table 6.1 Material parameters used for numerical modeling (Crosby, 2005; Luangthip et al., 2016).

Rock unit	Elastic properties			Density	Strength properties	
	E (GPa)	K (GPa)	G (GPa)	ρ (g/cm^3)	c (MPa)	ϕ (°)
Upper Clastics	3.80	3.52	1.44	2.49	3.50	25.00
Upper Salt	3.60	13.90	10.40	2.89	5.00	49.70
Middle Clastics	0.70	0.65	0.27	2.15	0.56	23.00
Middle salt	4.00	13.90	10.40	2.14	6.00	51.60
Lower Clastics	0.65	0.54	0.25	2.18	0.38	5.00
Lower Salt: $C_{\%}$ = 0%	2.48	11.64	6.59	2.16	4.46	46.48
Lower Salt: C% = 20%	1.53	9.15	4.24	2.05	3.11	46.48
Lower Salt: C% = 40%	0.95	7.20	2.73	1.94	2.17	46.48
Lower Salt: C% = 60%	0.59	5.66	1.76	1.82	1.51	46.48
Lower Salt: C% = 80%	0.36	4.46	1.13	1.71	1.06	46.48
Lower Salt: C% =100%	0.22	3.51	0.73	1.60	0.74	46.48

Table 6.2 Creep properties of the rock salt with various carnallite contents (Wilalak and Fuenkajorn, 2016).

Parameters	$C_{\%}$ (%)					
	0	**20**	**40**	**60**	**80**	**100**
Elastic modulus, E_1 (GPa)	2.48	1.53	0.95	0.59	0.36	0.22
Spring constant in visco-elastic phase, E_2 (GPa)	2.22	1.58	1.12	0.80	0.57	0.40
Visco-plastic coefficient in steady-state phase, η_1 (GPa.day)	45.16	21.12	9.88	4.62	2.16	1.01
Visco-elastic coefficient in transient phase, η_2 (GPa.day)	1.29	0.74	0.42	0.24	0.14	0.08

6.4 Numerical results

The tensile stress and tensile strain after excavation at period of 50 years are determined in the middle of the roof (point A in Figures 6.1 to 6.3). Figure 6.4 shows tensile stress as a function of time under difference depths, room widths and carnallite contents. The tensile stress are constant with time and increase with depths and roof widths while under the same depth and width, the carnallite contents do not affect tensile stress. The example of tensile stress at 230 m depth and 8, 10, 12 m room widths in given in Figure 6.4. The results indicate that the tensile stress are 0.32, 0.48 and 0.63, respectively.

Figures 6.5 to.6.7 show tensile strain after excavation, they increase with time, depths and room widths but decrease when carnallite contents increase. Table 6.3 shows tensile stress and tensile strains for each case.

The distribution of the tensile stresses and compressive stresses in mine roof shown in Figures 6.8 to 6.10. The results indicate that the distribution of stresses is concentrated in the rock close to the mine excavation, and the influence of the excavation reduces with increasing distance from room. The tensile stress concentrates at the center of the roof. The maximum compressive stress are concentrated at the top of roof.

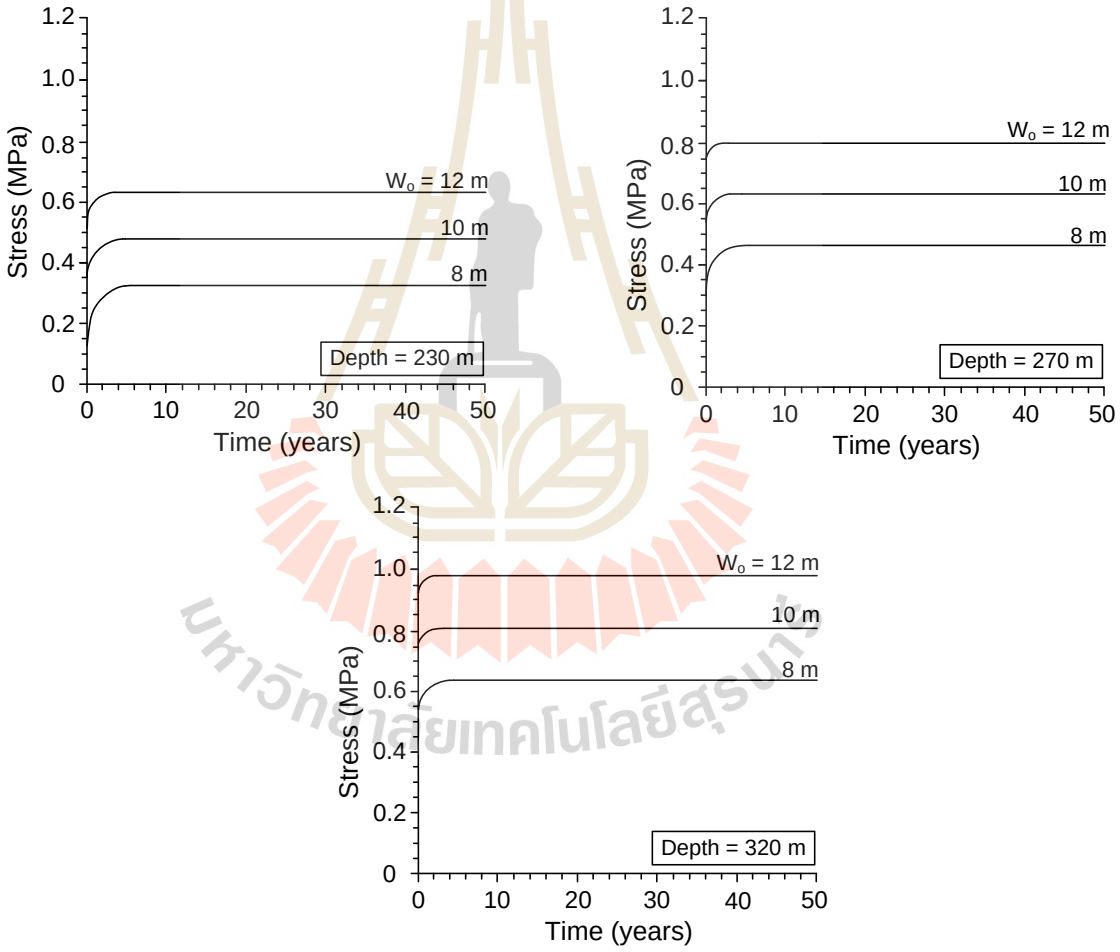

Figure 6.4 Tensile stresses as a function of time for 50 years excavations under various depths and room widths.

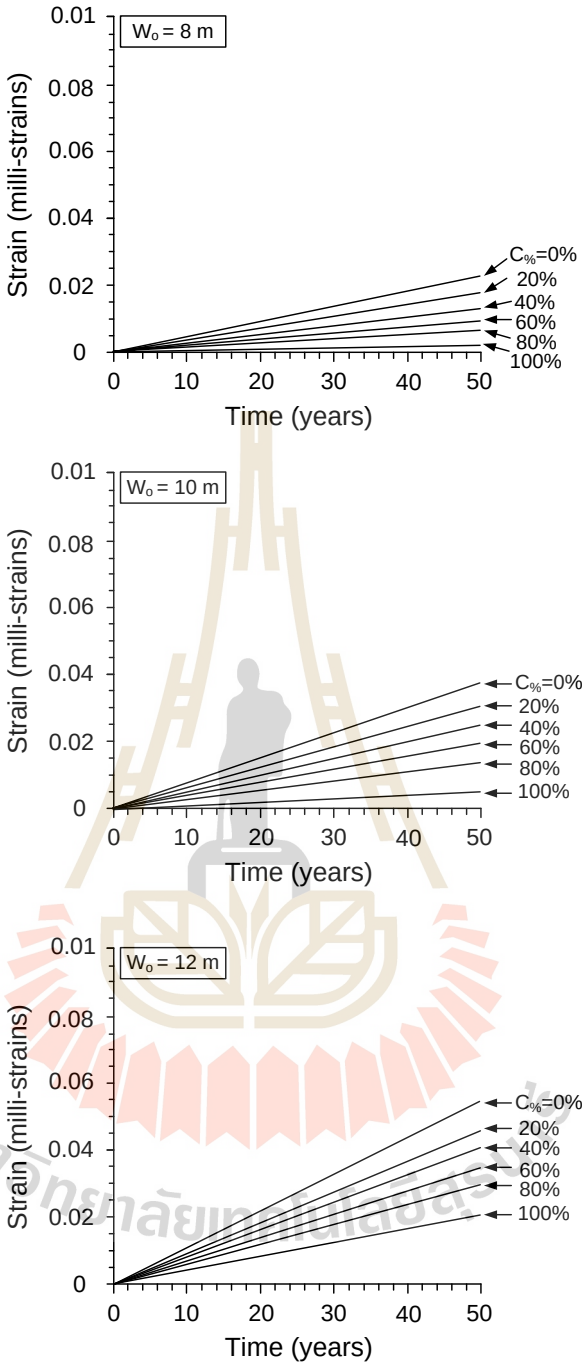

Figure 6.5 Tensile strains under various room widths for depth 230 m as a function of time for 50 years excavations.

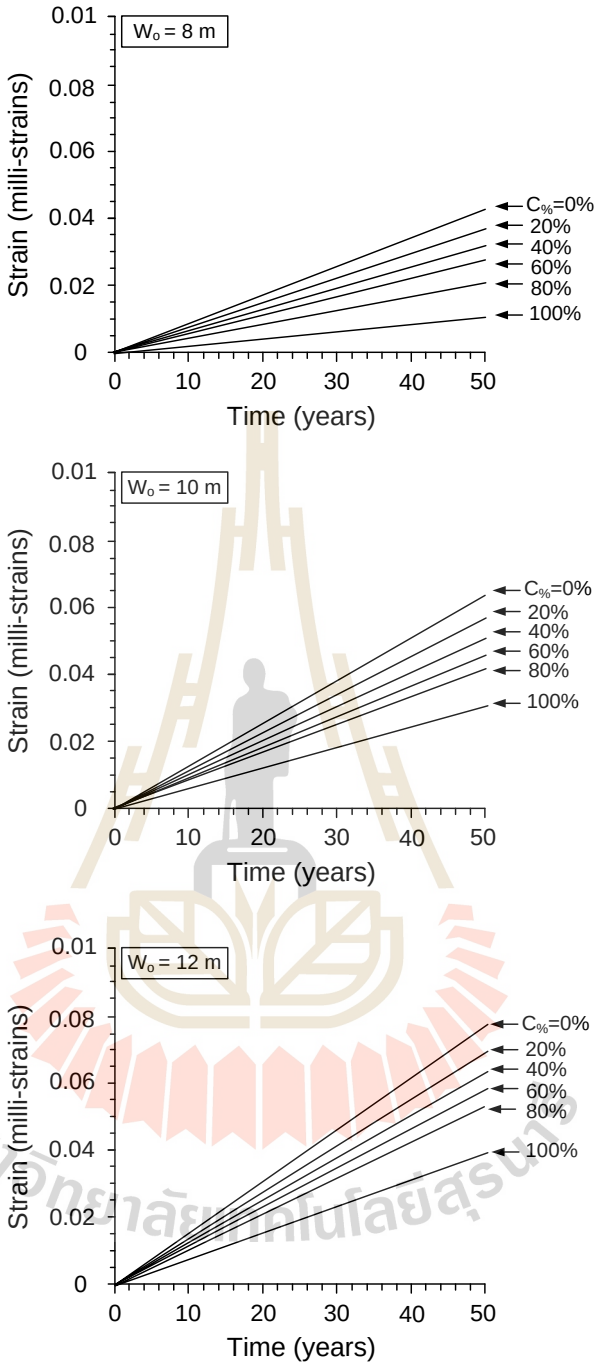

Figure 6.6 Tensile strains under various room widths for depth 270 m as a function of time for 50 years excavations.

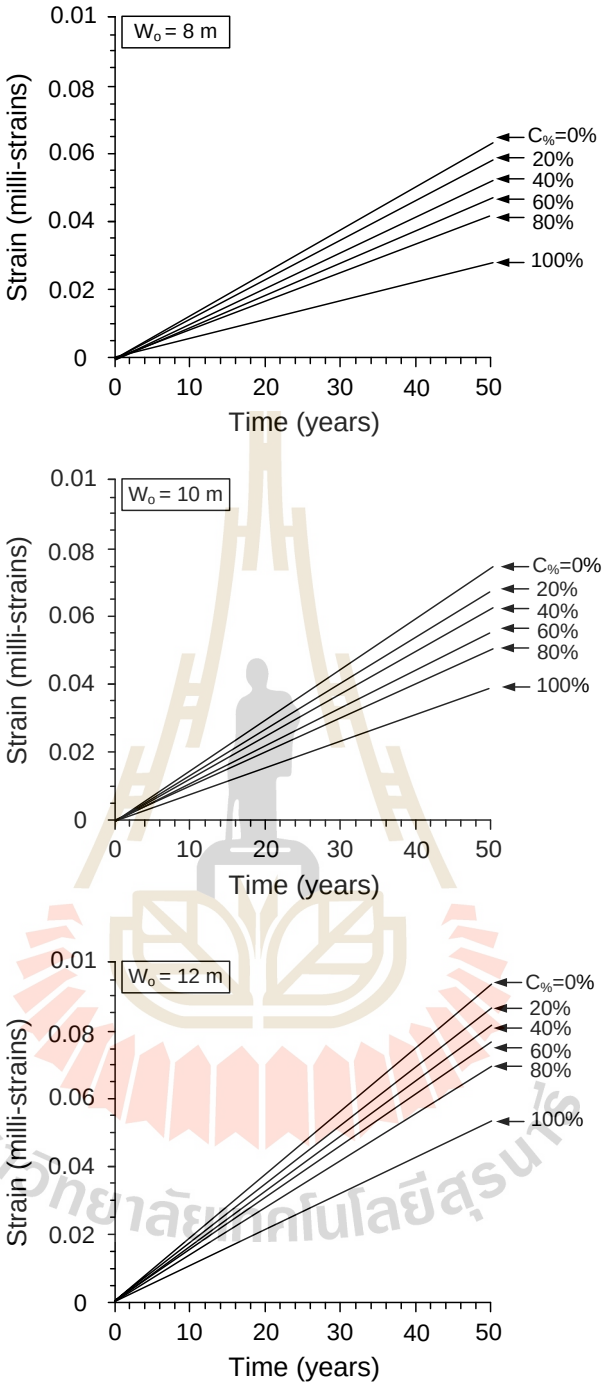

Figure 6.7 Tensile strains under various room widths for depth 320 m as a function of time for 50 years excavations.

Table 6.3 Simulation results for period 50 years.

Depths (m)	**Room widths (m)**	**$C_{\%}$ (%)**	**σ_t (MPa)**	**ε_t milli-strains**
230	8	0	0.32	0.00012
		20	0.32	0.00065
		40	0.32	0.00093
		60	0.32	0.00130
		80	0.32	0.00170
		100	0.32	0.00220
	10	0	0.48	0.00053
		20	0.48	0.00140
		40	0.48	0.00190
		60	0.48	0.00250
		80	0.48	0.00300
		100	0.48	0.00370
	12	0	0.63	0.00210
		20	0.63	0.00300
		40	0.63	0.00350
		60	0.63	0.00410
		80	0.63	0.00460
		100	0.63	0.00540
270	8	0	0.46	0.00100
		20	0.46	0.00210
		40	0.46	0.00270
		60	0.46	0.00320
		80	0.46	0.00370
		100	0.46	0.00420

มหาวิทยาลัยเทคโนโลยีสุรนารี

Table 6.3 Simulation results for period 50 years (con.).

Depths (m)	**Room widths (m)**	**$C_{\%}$ (%)**	**σ_t (MPa)**	**ε_t milli-strains**
270	10	0	0.63	0.00302
		20	0.63	0.00420
		40	0.63	0.00460
		60	0.63	0.00510
		80	0.63	0.00570
		100	0.63	0.00630
	12	0	0.80	0.00390
		20	0.80	0.00530
		40	0.80	0.00580
		60	0.80	0.00630
		80	0.80	0.00690
		100	0.80	0.00770
320	8	0	0.64	0.00280
		20	0.64	0.00420
		40	0.64	0.00470
		60	0.64	0.00520
		80	0.64	0.00580
		100	0.64	0.00630
	10	0	0.80	0.00380
		20	0.80	0.00500
		40	0.80	0.00550
		60	0.80	0.00620
		80	0.80	0.00670
		100	0.80	0.00740

มหาวิทยาลัยเทคโนโลยีสุรนารี

Table 6.3 Simulation results for period 50 years (con.).

Depths (m)	**Room widths (m)**	**$C_{\%}$ (%)**	**σ_t (MPa)**	**ε_t milli-strains**
320	12	0	0.98	0.00530
		20	0.98	0.00690
		40	0.98	0.00750
		60	0.98	0.00810
		80	0.98	0.00860
		100	0.98	0.00930

มหาวิทยาลัยเทคโนโลยีสุรนารี

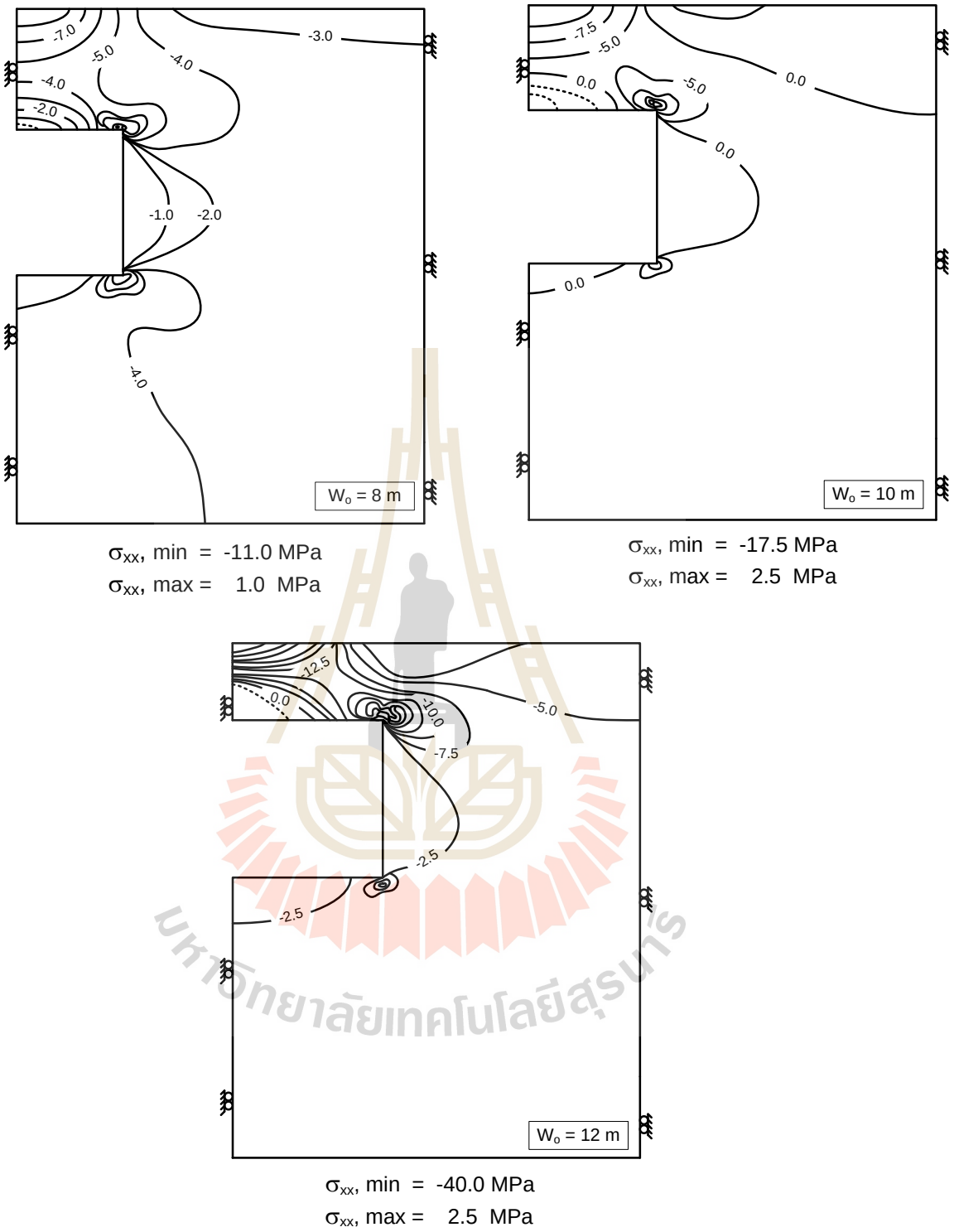

Figure 6.8 Examples of stress distribution in mine roof for depth 230 m.

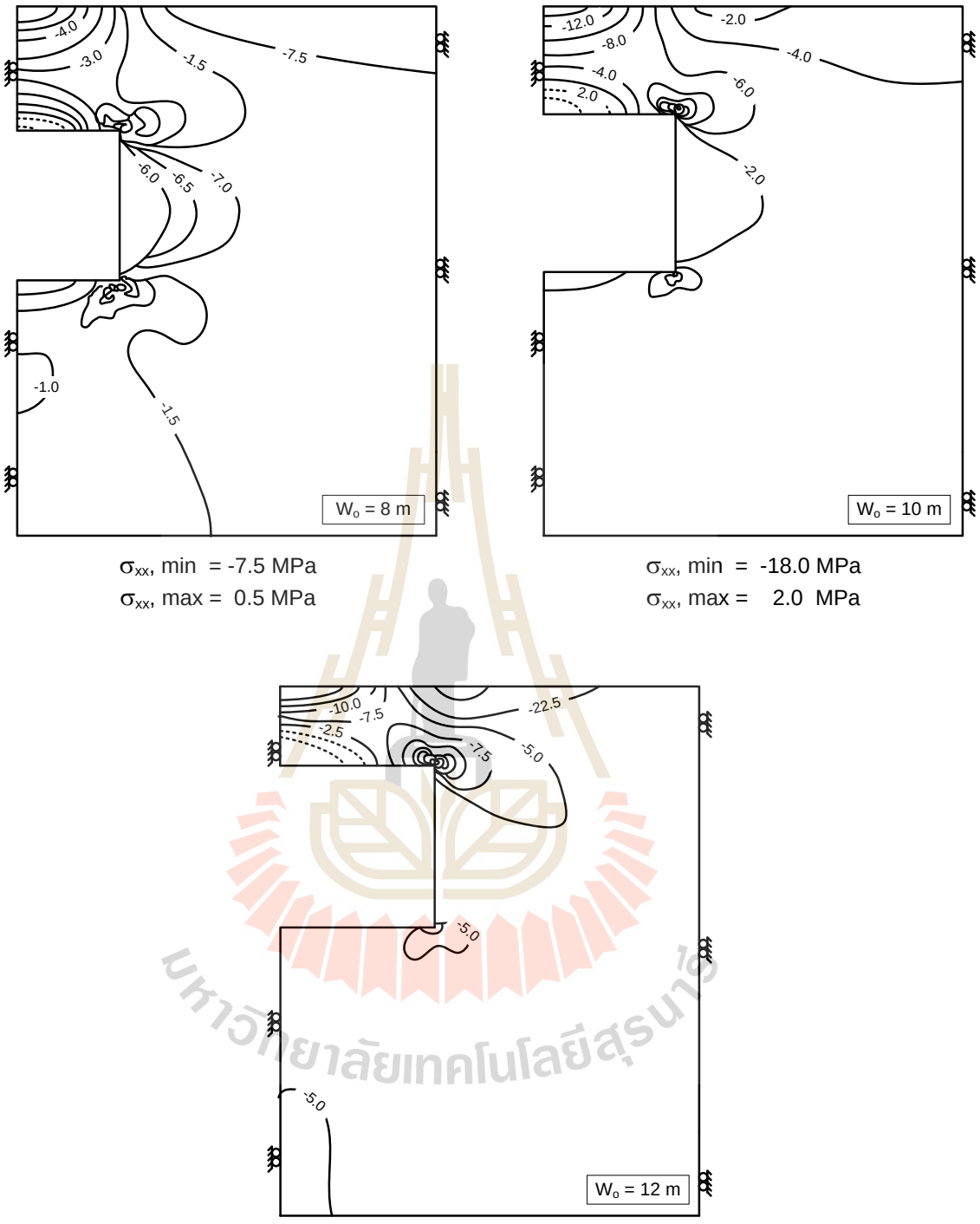

σ_{xx}, min = -7.5 MPa
σ_{xx}, max = 0.5 MPa

σ_{xx}, min = -18.0 MPa
σ_{xx}, max = 2.0 MPa

σ_{xx}, min = -25.0 MPa
σ_{xx}, max = 2.5 MPa

Figure 6.9 Examples of stress distribution in mine roof for depth 270 m.

มหาวิทยาลัยเทคโนโลยีสุรนารี

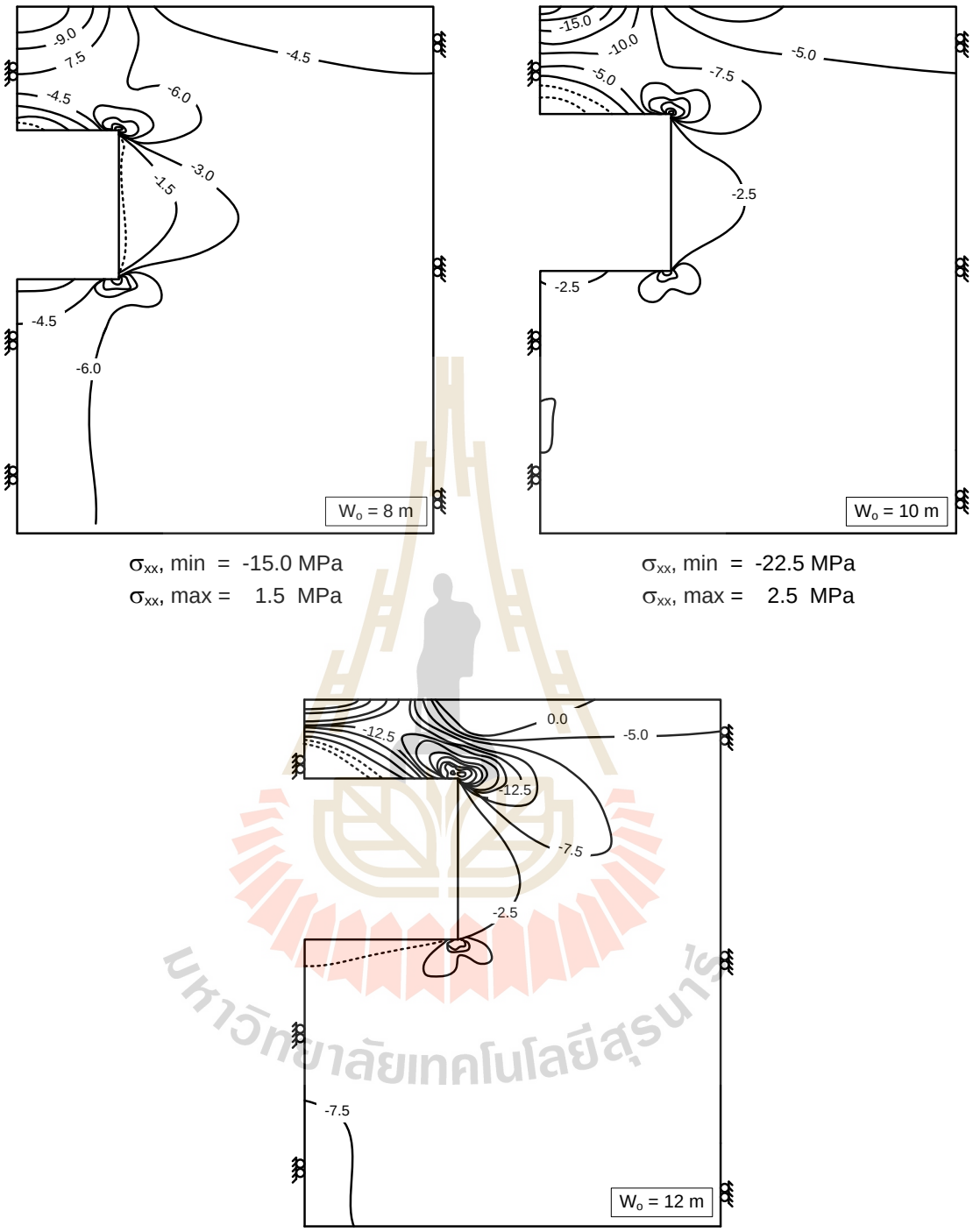

σ_{xx}, min = -15.0 MPa
σ_{xx}, max = 1.5 MPa

σ_{xx}, min = -22.5 MPa
σ_{xx}, max = 2.5 MPa

σ_{xx}, min = -55.0 MPa
σ_{xx}, max = 2.5 MPa

Figure 6.10 Examples of stress distribution in mine roof for depth 320 m.

CHAPTER VII

STADUP TIME OF MINE ROOF PREDICTION

7.1 Introduction

This chapter describes the application of the simulations of mine roof in rock salt obtained from Chapter VI to calculate the factor of safety (F.S.) from the strain energy criterion for predicted standup time of mine roof under different depths, room widths and carnallite contents in determined.

7.2 Factor of safety calculation for prediction standup time

The simulations of the mine roof in rock salt shown in Chapter VI is used to calculate the roof stresses combining with the strain energy criterion to determine the critical tensile strain that the roof can sustain before failure occurs. By substituting the critical strain into the strain-time curves the standup time can be predicted.

The strain energy from laboratory test from equation (5.8) and the strain energy of the simulations are used to calculate the factor of safety in the middle of the roof. The maximum standup time before support installation of mine roof can be calculated as:

$$F.S = W_t / W \tag{7.1}$$

where W_t is the strain energy from four-point bedding test, and W is the strain energy obtained from numerical model. For this demonstration F.S. is taken as 1.0.

Figures 7.1 to 7.3 show strain energy from simulation results as a function of standup time. The strain energy of simulation are used to calculate the factor of safety which calculated from equation (7.1), as shown in Table 7.1. The figures above show the calculated standup time before failure occurs. The horizontal dotted lines are obtained for the carnallite contents ranging from 0%, 20%, 40%, 60%, 80% and 100% which are calculated from equation (5.8). The vertical dotted lines show the maximum standup time of mine roof under different depths, room widths and carnallite contents. The results indicate that the standup time increases when depths, room widths and carnallite contents decrease.

Figures 7.4 to 7.6 show the maximum tensile strain as a function of standup time at depths are 230, 270 and 320 m under different room widths. By comparison with the strain energy criterion of test results, cross point (x) in the figures indicate maximum tensile strain and standup time of mine roof. The induced tensile strains increase with time, tensile strains decrease when depth, room width and carnallite contents increase.

มหาวิทยาลัยเทคโนโลยีสุรนารี

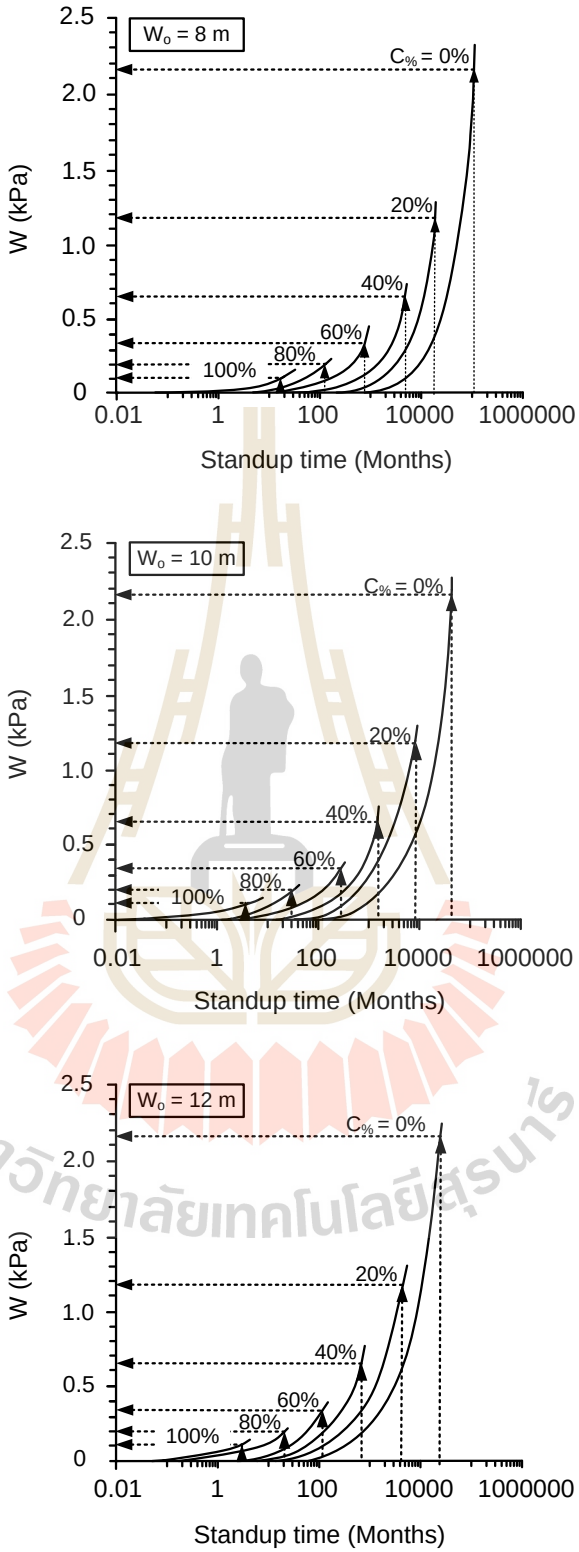

Figure 7.1 Strain energy of simulation results as a function of standup time for depth 230 m under different room widths and carnallite contents.

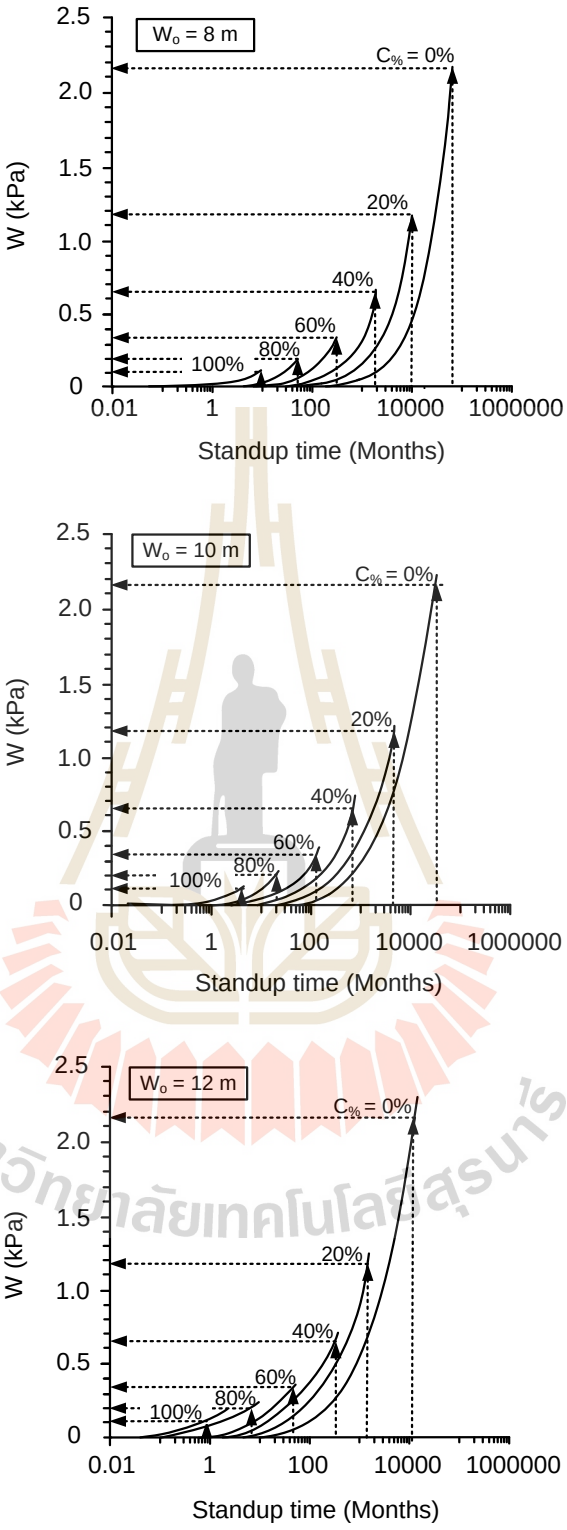

Figure 7.2 Strain energy of simulation results as a function of standup time for depth 270 m under different room widths and carnallite contents.

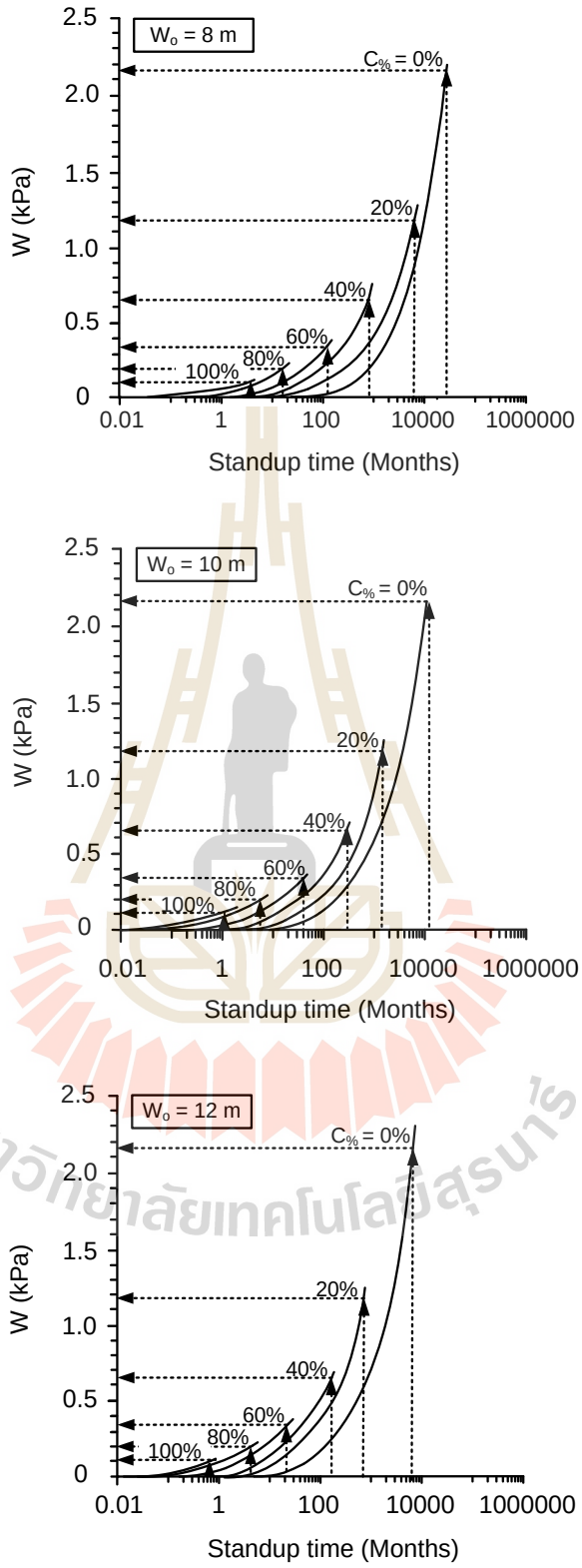

Figure 7.3 Strain energy of simulation results as a function of standup time for depth 320 m under different room widths and carnallite contents.

Table 7.1 Simulation results.

Depths (m)	Room widths (m)	$C_{\%}$ (%)	σ_t (MPa)	ε_t milli-strains	W (kPa)	W_t (kPa)	F.S
230	8	0	0.32	0.01355	2.17	2.17	1
		20	0.32	0.00735	1.18	1.18	1
		40	0.32	0.00405	0.65	0.65	1
		60	0.32	0.0022	0.35	0.35	1
		80	0.32	0.00125	0.20	0.20	1
		100	0.32	0.00066	0.11	0.11	1
	10	0	0.48	0.00904	2.17	2.17	1
		20	0.48	0.00492	1.18	1.18	1
		40	0.48	0.00271	0.65	0.65	1
		60	0.48	0.00145	0.35	0.35	1
		80	0.48	0.00085	0.20	0.20	1
		100	0.48	0.00045	0.11	0.11	1
	12	0	0.63	0.00689	2.17	2.17	1
		20	0.63	0.00375	1.18	1.18	1
		40	0.63	0.00206	0.65	0.65	1
		60	0.63	0.00111	0.35	0.35	1
		80	0.63	0.00064	0.20	0.20	1
		100	0.63	0.00036	0.11	0.11	1
270	8	0	0.46	0.00943	2.17	2.17	1
		20	0.46	0.00512	1.18	1.18	1
		40	0.46	0.00282	0.65	0.65	1
		60	0.46	0.0015	0.35	0.35	1
		80	0.46	0.00086	0.20	0.20	1
		100	0.46	0.00046	0.11	0.11	1

มหาวิทยาลัยเทคโนโลยีสุรนารี

Table 7.1 Simulation results (con.).

Depths (m)	Room widths (m)	$C_{\%}$ (%)	σ_t (MPa)	ε_t milli-strains	W (kPa)	W_t (kPa)	F.S
270	10	0	0.63	0.0069	2.17	2.17	1
		20	0.63	0.00374	1.18	1.18	1
		40	0.63	0.00207	0.65	0.65	1
		60	0.63	0.0011	0.35	0.35	1
		80	0.63	0.00062	0.20	0.20	1
		100	0.63	0.00036	0.11	0.11	1
	12	0	0.8	0.00543	2.17	2.17	1
		20	0.8	0.00296	1.18	1.18	1
		40	0.8	0.00162	0.65	0.65	1
		60	0.8	0.00087	0.35	0.35	1
		80	0.8	0.0005	0.20	0.20	1
		100	0.8	0.00028	0.11	0.11	1
320	8	0	0.64	0.00678	2.17	2.17	1
		20	0.64	0.00364	1.18	1.18	1
		40	0.64	0.00202	0.65	0.65	1
		60	0.64	0.00108	0.35	0.35	1
		80	0.64	0.00062	0.20	0.20	1
		100	0.64	0.00035	0.11	0.11	1
	10	0	0.8	0.00543	2.17	2.17	1
		20	0.8	0.00292	1.18	1.18	1
		0	0.8	0.00543	2.17	2.17	1
		20	0.8	0.00292	1.18	1.18	1
		40	0.8	0.00163	0.65	0.65	1
		60	0.8	0.00087	0.35	0.35	1
		80	0.8	0.00051	0.20	0.20	1
		100	0.8	0.00028	0.11	0.11	1

มหาวิทยาลัยเทคโนโลยีสุรนารี

Table 7.1 Simulation results (con.).

Depths (m)	**Room widths (m)**	**$C_{\%}$ (%)**	**σ_t (MPa)**	**ε_t milli-strains**	**W (kPa)**	**W_t (kPa)**	**F.S**
320	12	0	0.98	0.0068	2.17	2.17	1
		20	0.98	0.00366	1.18	1.18	1
		40	0.98	0.00203	0.65	0.65	1
		60	0.98	0.0011	0.35	0.35	1
		80	0.98	0.00061	0.20	0.20	1
		100	0.98	0.00033	0.11	0.11	1

มหาวิทยาลัยเทคโนโลยีสุรนารี

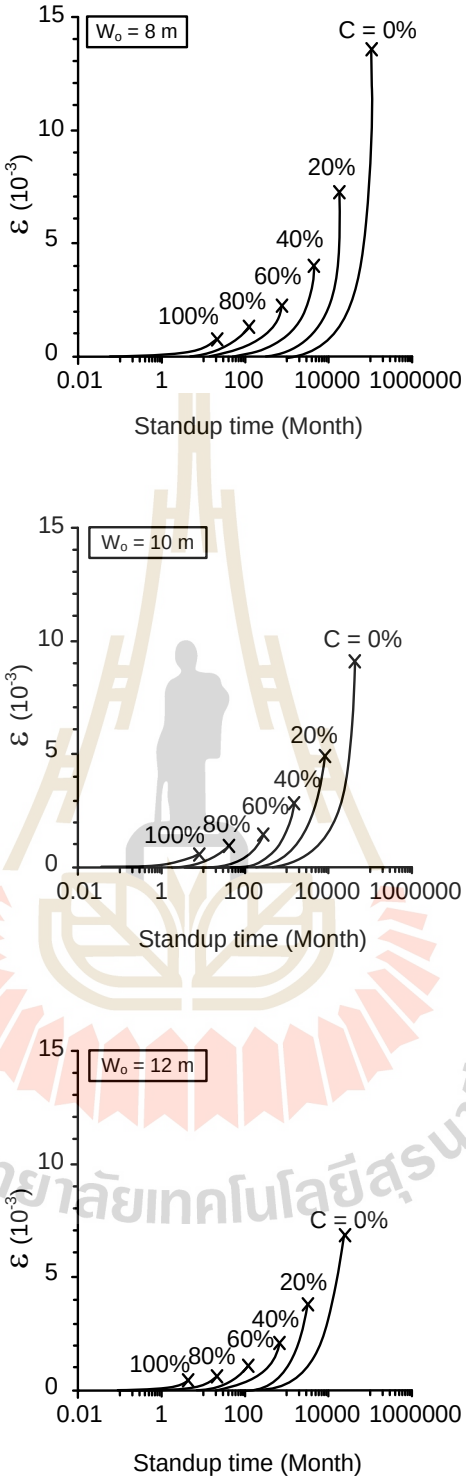

Figure 7.4 Maximum tensile strain as a function of time at depth 230 m under different room widths.

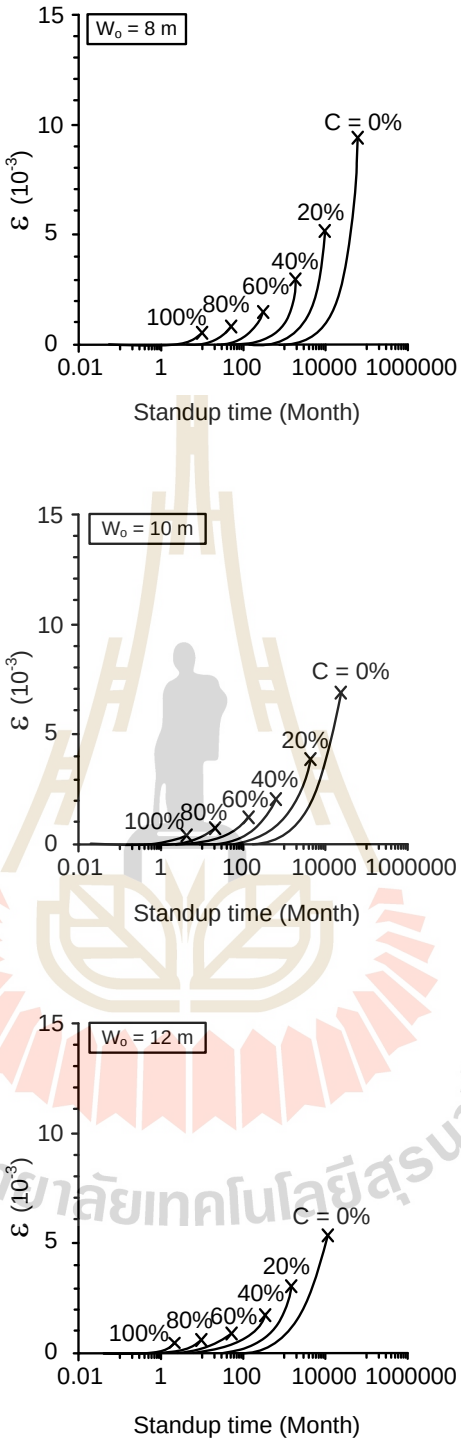

Figure 7.5 Maximum tensile strain as a function of time at depth 270 m under different room widths.

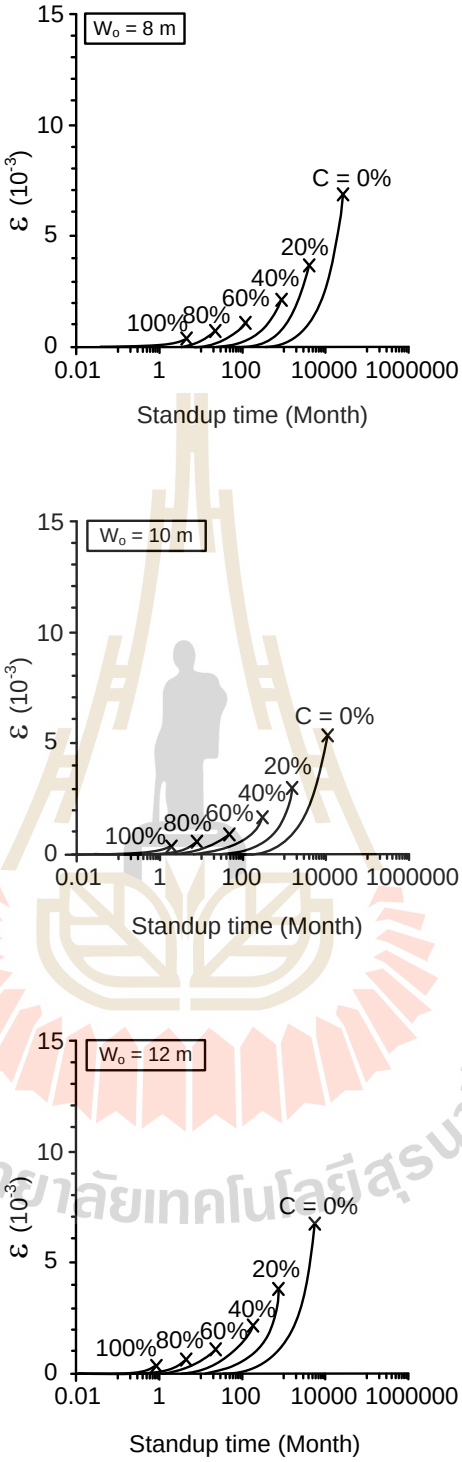

Figure 7.6 Maximum tensile strain as a function of time at depth 320 m under different room widths.

7.3 Standup time of the mine roof

An empirical equation is proposed to predict the standup time of the mine roof under different depths and carnallite contents for room widths are 8, 10 and 12 m. For the Maha Sarakham salt they are defined in Table 7.2. The standup time of the mine roof can be calculated using the equation.

$$\text{Standup time} = \exp\text{-}[(C_{\%}+((\varphi \cdot \text{Depth})- \varphi'))/\xi] \quad (7.2)$$

where φ, φ' and ξ are empirical constants

The results show that as the carnallite contents increase, the standup time of the mine roof logarithmically reduces, as shown in Figure 7.7. The deeper mine opening (higher tensile stress in the roof) leads to the shorter stability duration. The effect of the mine depths tends to be linear. Table 7.3 shows the standup time of mine roof under difference depths, room widths and carnallite contents.

Table 7.2 Parameters calibrated from results simulate.

Room widths (m)	**Parameters**			**R^2**
	φ	**φ'**	**ξ**	
8	0.208	181.65	11.97	0.980
10	0.211	172.43	12.24	0.982
12	0.213	164.56	12.06	0.976

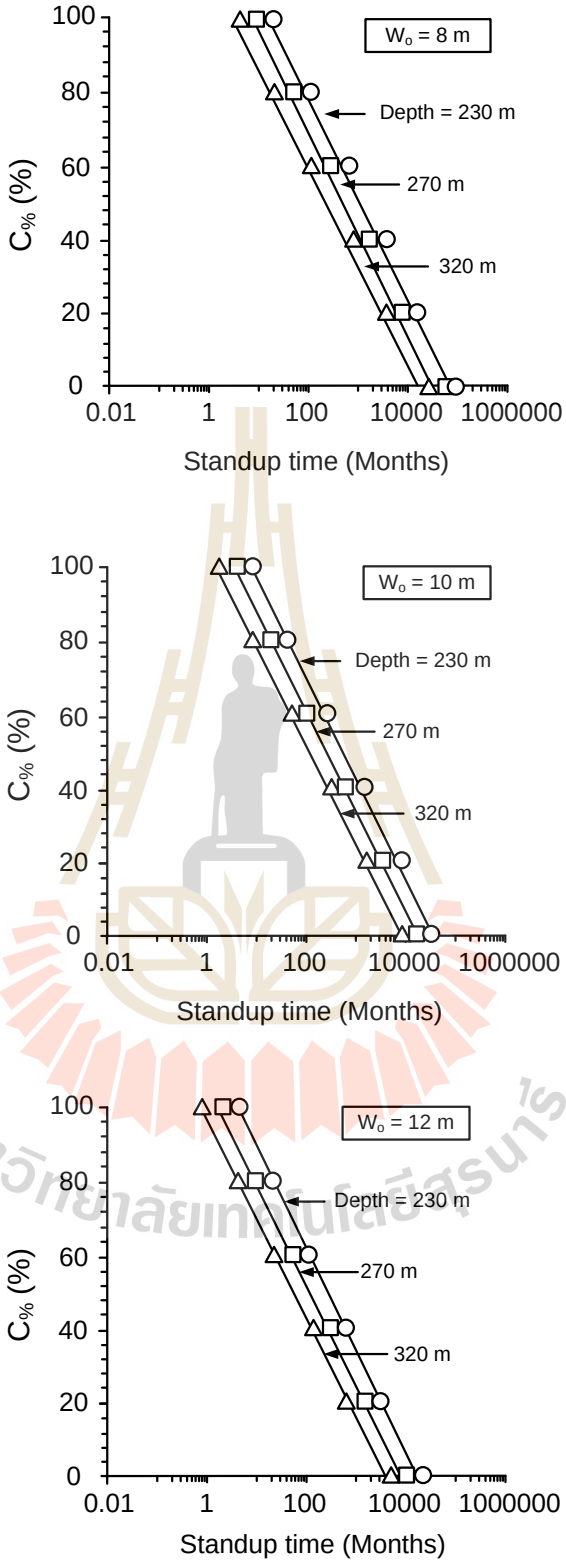

Figure 7.7 Standup time of carnalitite roof under different depths.

Table 7.3 Standup time of mine roof under difference depths, room widths and carnallite contents.

Depths (m)	**Room widths (m)**	**$C_{\%}$ (%)**	**Standup time (Month)**
230	8	0	91468
		20	15233
		40	3787
		60	634
		80	102
		100	17
	10	0	40172
		20	7642
		40	1408
		60	262
		80	41
		100	8
	12	0	21872
		20	3142
		40	612
		60	113
		80	21
		100	4
270	8	0	52813
		20	8102
		40	1624
		60	272
		80	46
		100	9

มหาวิทยาลัยเทคโนโลยีสุรนารี

Table 7.3 Standup time of mine roof under difference depths, room widths and carnallite contents (con.).

Depths (m)	**Room widths (m)**	**$C_{\%}$ (%)**	**Standup time (Month)**
270	10	0	20623
		20	3428
		40	628
		60	104
		80	19
		100	4
	12	0	10172
		20	1522
		40	297
		60	52
		80	9
		100	2
320	8	0	25058
		20	3871
		40	783
		60	112
		80	20
		100	5
	10	0	10578
		20	1629
		40	287
		60	46
		80	8
		100	2

มหาวิทยาลัยเทคโนโลยีสุรนารี

Table 7.3 Standup time of mine roof under difference depths, room widths and carnallite contents (con.).

Depths (m)	**Room widths (m)**	**$C_{\%}$ (%)**	**Standup time (Month)**
320	12	0	4622
		20	627
		40	136
		60	22
		80	4.3
		100	0.8

มหาวิทยาลัยเทคโนโลยีสุรนารี

CHAPTER VII

DISCUSSIONS, CONCLUSIONS AND RECOMMENDATIONS FOR FUTURE STUDIES

8.1 Discussions

This section discusses the key issues relevant to the reliability of the test schemes and the adequacies of the test results. Comparisons of the results and findings from this study with those obtained elsewhere under similar test conditions have also been made.

- The numbers of the test specimens seem adequate for fitting with the creep models, as evidenced by the good coefficients of correlation for all loading rates and carnallite contents.

- The test results in terms of the tensile strength and loading rate seem to be reliable. The results is agreed reasonably well with the related test results on the Maha Sarakham salt obtained by Wisetsaen et al. (2015).

- The specimens size used in this study are relatively small. Recognizing the size effects on the rock strengths (Jaeger et al., 2007), larger specimens should be used in summary the strengths obtained here under all test schemes would overestimate the strength of the salt under in-situ condition due to the scale effect. Nevertheless, the issue of the size effect would not change the main conclusions drawn here that the tensile strengths decrease when the carnallite contents increase. The

strength also increase with loading rate. The strain energy determined here is by assuming that the stress-strain relations under various carnallite content are non-linear. Because the strain energy of the tested specimens decreases with increasing carnallite contents.

- The loading rate used in this study is relatively high as compared to those of the salt around the mine roof caverns. The loading rate here complies with that of the ASTM (D7012-04) standard practice. It is recognized that rock under high loading rate would give higher tensile strength and stiffness than that under lower loading rates (Zhang and Wong, 2014 and Wisetsaen et al., 2015). As a results the tensile strengths and their corresponding criteria derived here may also over-estimate those of the in-situ salt where it is likely to subject to much lower loading rates.

8.2 Conclusions

All objectives and requirements of this study have been met. The results of the laboratory testing and analyses can be concluded as follows:

The effect of carnallite content and loading rate on the rock tensile strength is assessed under four constant rates from 0.045 N/s to 45 N/s. The results show that the tensile strengths decrease when the carnallite contents increase. The tensile strength also increases with increasing loading rate.

The strength results are used to develop a strength criterion in form of the strain energy density as a function of the carnallite content. Obtaining the specimen strengths under a wide range of loading rates allows a rigorous calibration of the strain energy equation. The observed time-dependent deformations are used to develop a governing

equation based on the Maxwell model. The results indicate that the elastic and viscosity parameters increases when the carnallite contents decrease

Numerical simulations of the mine roof under different depths, room widths and carnallite contents provide the maximum tensile stress in the middle of the salt roof. The simulation results also give the increase with time of the induced tensile strains based on the Burgers model. The distribution of stresses is concentrated in the rock close to the mine excavation, and the influence of the excavation reduces with increasing distance from room. The tensile stress concentrates at the center of the roof. The maximum compressive stress are concentrated at the top of roof. The roof stress and the critical strain for each mine depth and room width are compared with the strain energy criterion to determine the maximum duration (standup time) under which the roof will remain stable. The similar approach can also be performed for different mine widths, depths and roof thickness.

8.3 Recommendations for future studies

The test specimens here are relatively small. Testing on larger specimens is desirable to confirm the research findings. Verification of the four-point bending test proposed concept should be tested under a wider range of salt from other sources. The variation of the strength results is probably due to the high intrinsic variability of the test specimens. Even though halite and carnallite are the main mineral compositions, some trace inclusions (e.g., clay minerals and anhydrite) may cause the strength variation. It should be noted that different creep model can also be used to describe the time-dependency of the tensile deformations obtained from the bending testing. The Maxwell model is used here primarily because it can isolate the elastic (instantaneous)

response from the visco-plastic deformation. More test specimens under a wider range of the loading rates would enhance the representativeness of the governing equation. The study effect of carnallite content in underground mine roof for calculated the maximum unsupported span and standup time of the potash mine roof by used to FLAC software. It is a preliminary prediction only because real conditions may take into account a variety of reasons, such as structural geology, depth, water pressure and shear strength, etc.

REFERENCES

ASTM C293–02. Standard test method for flexural strength of concrete (Using simple beam with center-point loading). In **Annual Book of ASTM Standards**. (Vol. 04.08). West Conshohocken: American Society for Testing and Materials.

ASTM D6272-10. Standard test method for flexural properties of unreinforced and reinforced plastics and electrical insulating material by four-point bending. In **Annual Book of ASTM standard**. (Vol. 04.08). West Conshohocken: American Society for Testing and Materials.

Bacher, K. (1949). Determination of the elastic constants of rocks by supersonics. **Erdoel u. Kohle.** 2(4): 125-127.

Batuecas, T. and Carreirra, M. (1955). High-precision pycnometric investigations on pure substances. **Anales de la Real Sociedad Española de Física y Química.** 51B: 311-320.

Bauer, S. J., Ehgartner, Levin, B. L., and Linn, J. K. (1998). Waste disposal in horizontal solution mined caverns-considerations of site location, cavern stability, and development considerations. In **Proceedings of SMRI Fall Meeting.** Rome, Italy.

Berenbaum, R. and Brodie, I. (1959). The tensile strength of coal. **Journal of the Institute of Fuel.** 32: 320-327.

Birch, F., Schairer, J. F., and Spicer, H. C. (1942). **Handbook of Physical Constants.** Geological Society of America Special Papers. 36: 25-32.

Crosby, K. S. (2005). Overview of the geology and resources of the Udon Potash (sylvinite) deposits, Udon Thani province, Thailand. In **Proceedings of International Conference on Geology, Geotechnology and Mineral Resources of Indochina** (pp. 283-299). Khon Kaen, Thailand.

Evans, I. (1961). The tensile strength of coal. **Colliery Engineering.** 38: 428-434.

Fairhurst, C. (1961). Laboratory measurement of some physical properties of rock. In **Proceedings of the 4th U.S. Symposium on Rock Mechanics (USRMS**), 30 March-1 April 1961, University Park, Pennsylvania.

Forster, J. (1967) Stability investigations applied to mining of evaporates. **Ph.D. thesis, University of Newcastle upon Tyne.**

Forsythe, W. Z. (1954). **Smithsonian Physical Tables.** Smithsonian Miscellaneous Collections. 120: 294-320.

Fuenkajorn, K. and Daemen, J. J. K. (1988). Borehole Closure in Salt, **Technical Report NUREC/CR-5243**, prepared for the U. S. Nuclear Regulatory Commission, Washington, D. C.

Han, G., Bruno, M. S., Lao, K., Young, J., and Dorfmann, L. (2006). Gas Storage and Operations in Single-Bedded Salt Caverns: Stability Analyses. **SPE Gas Technology Symposium in Calgary.** Alberta, Canada.

Hawthorne, F.S. and Ferguson, R.B. (1975). Anhydrous sulphates. II. Refinement of the crystal structure of anhtdrite. **Canadian Mineralogist.** 13: 289-292.

Heiland, C. A. (1940). **Geophysical Exploration.** Prentice-Hall. Inc., New York.

Hodgman, C. D., Weast, R. C., and Selby, S. M. (1955-1956). **Handbook of Chemistry and Physics.** Chemical Rubber Publishing Co., Cleveland, Ohio.

Hurlbut, C. H. and Klein, C. (1977). Manual of mineralogy. **19th Edition**. Wiley, New York.

Itasca (1992). **FLAC-Fast Langrangian Analysis of Continua, Version 4.0**, **User Manual**. Itasca Consulting Group Inc., Minnespolis, MN, USA.

Jaeger, J. C., Cook, N. G. W., and Zimmerman, R. W. (2007). **Fundamentals of Rock Mechanics Fourth Edition.** Blackwell publishing, Oxford.

Johnston, H. L. and Hutchison, D. A. (1942). Density of sodium chloride. **Physical Review.** 62: 32-36.

Klein, C., Hurlbut, C. S., and Dana, J. D. (1998). **Manual of Mineralogy**. John Wiley and Sons Inc. Wiley, New York.

Luangthip, A., Khamrat, S., and Fuenkajorn, K. (2016). Effects of carnallite contents on stability and extraction ratio of potash mine. In **Proceedings of the 9th Asian Rock Mechanics Symposium.** October 18-21, Bali, Indonesia.

Liu, L. F., Pei, J. L., Ma, K., Zhou, H., and Hou, Z. (2010). Underground storage of CO_2 and energy. In **Proceedings of the Sino-German Conference** (pp. 105-112). July 2010, Beijing, China.

Mellegard, K. D., Robert, L. A., and Callahan, G. D. (2012). Effect of sylvite content on mechanical properties of potash. **Mechanical Behavior of Salt VII-Berest, Ghoreychi, Hadj-Hassen and Tijani** (pp. 71-79). Taylor and Francis Group, London.

National Research council of the U.S.A. (1929). **International Critical Tables**. McGraw-Hill Book Company, Inc., New York.

Obert, L., Duvall, W. I. (1967). **Rock Mechanics and the Design of Structures in Rock.** John Wiley, New York.

Obert, L., Windes, S. L. and Duvall, W. I. (1946). Standardized tests for determining the physical properties of mine rock. **US Bur. Mines Rep. Invest**. 3891.

Phueakphum, D., Fuenkajorn, K. and Walsri, C. (2013). Effects of intermediate principal stress on tensile strength of rocks. **International Journal of Fracture**. 181: 163-175.

Pomeroy, C. D., and Morgans, W. T. A. (1956). The tensile strength of coal. **British Journal of Applied Physics.** 7: 243-6.

Price, N. J., and Cosgrove, J. W. (1964). A study of the time-strain behavior of coal measure rocks. **International Journal of Rock Mechanics and Mining Sciences**. 1(2): 277-303.

Sathe, N. V., Phalniker, N. L., and Bhide, B. V. (1945). Dielectric constants of inorganic salts. **Journal of the Indian Chemical Society.** 22: 29-36.

Schlemper, E.O., Sen Gupta, P.K. and Zoltai, T. (1985). Refinement of the structure of carnallite, $Mg{\cdot}(H_2O)_6KCl_3$. **American Mineralogist**. 70(11-12): 1309-1313.

Snyder, V. W. (1983). Analysis of beam building using fully grouted roof bolts. In **Proceedings of the International Symposium on Rock Bolting** (pp. 187-194). Abisko, Sweden.

Stimpson, B. and Ahmed, M. (1992). Failure of a linear voussoir arch: a laboratory and numerical study. **Canadian Geotechnical Journal.** 29: 188-194.

Straumanis, M. Z. (1953). Density determinations by a modified suspension method, X-ray molecular weight and soundness of sodium Chlorides. **American Mineralogist.** 38: 662-670.

มหาวิทยาลัยเทคโนโลยีสุรนารี

Suwanich, P. (2007). Potash-evaporite deposits in Thailand. In **Proceedings of the International Conference on Geology of Thailand** (pp. 252-262). 21-22 November 2007, Department of Mineral Resources, Thailand.

Swift, G. M and Reddish, D. J. (2001). Underground excavations in rock salt. **Geotechnical and Geological Engineering.** 23: 17–42.

Wang, T., Yan, X., Yang, X., and Jiang, T. (2012). Roof stability evaluation of bedded rock salt cavern used as underground gas storage. **Research Journal of Applied Sciences, Engineering and Technology.** 4(20): 4160-4170.

Wang, T., Yang, C., Shi, X., Ma, H., Li, Y., Yang, Y., and Daemen, J.J.K. (2015). Failure analysis of thick interlayer from leaching of bedded salt caverns. **International Journal of Rock Mechanics and Mining Sciences.** 73: 175-183.

Warren, J. (1999). **Evaporites: Their evolution and economics** (pp. 235-239). Philadelphia: Blackwell Science.

Weinberger, R., Reches, Z., and Eidelman, A. (1994). Tensile properties of rock in four-point beam test under confining pressure. **Rock Mechanics.** 435-442.

Wendai, L. (2000). Regression analysis, linear regression and probit regression In 13 chapters. **SPSS for Windows: statistical analysis.** Publishing House of Electronics Industry. Beijing.

Weck, P. F., Kim, E., Jové-Colón, C. F. and Sassani, D. C. (2014). First-principles study of anhydrite, polyhalite and carnallite. **Chemical Physics Letters.** 594: 1-5.

Wilalak, N. and Fuenkajorn, K. (2016). Constitutive equation for creep closure of shaft and borehole in potash layers with varying carnallite contents. In **Proceedings**

of the 9th Asian Rock Mechanics Symposium. October 18-21, Bali, Indonesia.

Wisetsaen, S., Walsri, C., and Fuenkajorn, K. (2015). Effects of loading rate and temperature on tensile strength and deformation of rock salt. **International Journal of Rock Mechanics and Mining Sciences.** 73: 10-14

Yang, C., Wang, T., Qu, D.A., Ma, H., Li, Y., Shi, X., and Daemen, J.J.K. (2016). Feasibility analysis of using horizontal caverns for underground gas storage: A case study of Yunying salt district. **Journal of Natural Gas Science and Engineering.** 36: 252-266.

Yokoyama, T. A. (1988). A microcomputer-aided four-point test system for determining uniaxial stress-strain curves. **Journal of Testing and Evaluation.** 16: 198-204.

Zhang, X. and Wong, L. N. Y. (2014). Choosing a proper loading rate for bonded-particle model of intact rock. **International Journal of Fracture rock.** 189(2): 163-179.

มหาวิทยาลัยเทคโนโลยีสุรนารี

BIOGRAPHY

Miss Monyapat Chobsranoi was born on July 5, 1993 in Nakhon Ratchasima Province, Thailand. She received her Bachelor's Degree in Engineering (Geotechnology) from Suranaree University of Technology in 2016. For her post-graduate, she continued to study with a Master's degree in the Geological Engineering Program, Institute of Engineering, Suranaree university of Technology. During graduation, 2015-2016, she was a part time worker in position of research assistant at the Geomechanics Research Unit, Institute of Engineering, Suranaree University of Technology.

มหาวิทยาลัยเทคโนโลยีสุรนารี